

Evolution of the H β +[OIII] and [OII] luminosity functions and the [OII] star-formation history of the Universe up to $z \sim 5$ from HiZELS

A. A. Khostovan^{1*}, D. Sobral^{2,3,4}, B. Mobasher¹, P. N. Best⁵, I. Smail⁶, J. P. Stott⁷, S. Hemmati¹, H. Nayyeri⁸

¹Department of Physics & Astronomy, University of California, Riverside, United States of America

²Instituto de Astrofísica e Ciências do Espaço, Universidade de Lisboa, OAL, Tapada da Ajuda, PT1349-018 Lisboa, Portugal

³Departamento de Física, Faculdade de Ciências, Universidade de Lisboa, Edifício C8, Campo Grande, PT1749-016 Lisbon, Portugal

⁴Leiden Observatory, Leiden University, PO Box 9513, NL-2300 RA Leiden, the Netherlands

⁵SUPA, Institute for Astronomy, Royal Observatory of Edinburgh, Blackford Hill, Edinburgh, EH9 3HJ, UK

⁶Centre for Extragalactic Astrophysics, Durham University, South Road, Durham, DH1 3LE, UK

⁷Institute of Computational Cosmology, Durham University, South Road, Durham, DH1 3LE, UK

⁸Department of Physics & Astronomy, University of California, Irvine, United States of America

Released 2015 February 24

ABSTRACT

We investigate the evolution of the H β +[OIII] and [OII] luminosity functions from $z \sim 0.8$ to ~ 5 in multiple redshift slices using data from the High- z Emission Line Survey (HiZELS). This is the first time that the H β +[OIII] and [OII] luminosity functions have been studied at these redshifts in a self-consistent analysis. This is also the largest sample of [OII] and H β +[OIII] emitters (3484 and 3301 emitters, respectively) in this redshift range, with large co-moving volumes $\sim 1 \times 10^6 \text{ Mpc}^{-3}$ in two independent volumes (COSMOS and UDS), greatly reducing the effects of cosmic variance. The emitters were selected by a combination of photometric redshift and color-color selections, as well as spectroscopic follow-up, including recent spectroscopic observations using DEIMOS and MOSFIRE on the Keck Telescopes and FMOS on Subaru. We find a strong increase in L_* and a decrease in ϕ_* with increasing redshift up to $z \sim 2$ and $z \sim 5$ for H β +[OIII] and [OII] emitters, respectively. For H β +[OIII], this evolution then flattens by $z \sim 3$. We derive the [OII] star-formation history of the Universe since $z \sim 5$ and find that the cosmic SFRD rises from $z \sim 5$ to ~ 3 and then drops towards $z \sim 0$. We also find that our star-formation history is able to reproduce the evolution of the stellar mass density up to $z \sim 5$. When comparing the H β +[OIII] SFRDs to the [OII] and H α SFRD measurements in the literature, we find that there is a remarkable agreement, suggesting that the H β +[OIII] sample is dominated by star-forming galaxies at high- z rather than AGNs.

Key words: galaxies: evolution, galaxies: high-redshift, galaxies: luminosity function, mass function, cosmology: observations

1 INTRODUCTION

Our understanding of the mass assembly and star-formation processes of the Universe has improved greatly over the past few decades (for in-depth reviews, see Kennicutt & Evans 2012 and Madau & Dickinson 2014). We currently have evidence to show that the cosmic star-formation rate (SFR) peaked at $z > 1$ and that about half of the current stellar mass density had been assembled by that time

(e.g. Lilly et al. 1996; Hopkins & Beacom 2006; Karim et al. 2011; Sobral et al. 2013). However, many open questions remain. How fast did the star-formation rate density (SFRD) drop at $z > 2$? How has the population of star-forming galaxies changed over cosmic time? How does the evolution depend on the environment over cosmic time? To answer these questions, it is imperative that we use samples of star-forming galaxies that are low in contaminants and are well-defined in terms of selection methodology.

There are many different star-formation indicators and calibrations in the literature. Each indicator traces the star-

* E-mail: akhostov@gmail.com

formation activity in galaxies independently and with different timescales. The ultraviolet (UV) light from bright, young stars with masses $> 5 M_{\odot}$ traces the bulk of the young population with time scales of ~ 100 Myr. UV light of stars with masses $> 10 M_{\odot}$ ionize the gas along the line-of-sight, resulting in the absorption and then re-emission of photons seen as nebular (e.g., Lyman, Balmer, and Paschen series of the Hydrogen Atom) and forbidden emission lines (e.g., [OIII] & [OII]). The lifetimes for stars capable of ionizing the surrounding gas and dust to form the nebular and forbidden emission lines are on the scale of ~ 10 Myr, allowing for the measurement of the instantaneous star-formation rate. Other indicators include far-infrared emission coming from the heating of dust shrouding the hot, UV bright, young stars and the synchrotron emission in the radio coming from accelerated electrons in supernovae. For an in-depth review of the various indicators and calibrations, we refer the reader to reviews in the literature (e.g., Kennicutt 1998, Calzetti 2013).

Despite the different indicators that exists, one can not say that only one of the indicators is the “holy grail” of measuring the SFR of star-forming galaxies. However, using different tracers to map out the evolution of the cosmic SFR history is not the best solution either. This is because evolutionary studies based on samples selected in different ways and using different indicators/calibrations at different redshifts will be susceptible to complicated, strong biases and selection effects, which results in a significant scatter when combining all of them to probe the evolution of the cosmic SFR. Another issue is that most studies don’t probe sufficiently large volumes to overcome the effects of cosmic variance. Furthermore, the effects of correcting for dust extinction, especially for UV and optical studies, can result in large systematic uncertainties. One requires an indicator that can be used to probe from the low- z to the high- z Universe using a robust and consistent methodology to reduce the effects and biases that come from making assumptions and differing selection techniques.

Emission lines observed using narrow-band imaging techniques can provide an accurate and reliable sample of star-forming galaxies (e.g., Bunker et al. 1995; Fujita et al. 2003; Glazebrook et al. 2004; Ly et al. 2007; Villar et al. 2008; Geach et al. 2008; Sobral et al. 2013). The advantage of narrow-band imaging surveys is that they allow for the selection of emitters with a clean selection function by emission line flux and within a known narrow redshift range. This is because the filter width is quite narrow, such that any source brighter than expected from its broad-band magnitude is an emitter. Emission-line surveys via grism spectroscopy on the *HST* (e.g., Colbert et al. 2013) are also great accompaniments to narrow-band studies.

Most narrow-band surveys have focused on $\text{H}\alpha$ (e.g., Tresse et al. 2002; Fujita et al. 2003; Pascual 2005; Ly et al. 2007, 2011; Sobral et al. 2009, 2013) as it is a reliable star-formation indicator which is well-calibrated in the local universe and is only mildly affected by dust attenuation. The latest results of the High-Emission Line Survey (HiZELS, Geach et al. 2008; Sobral et al. 2009, 2012, 2013) have robustly traced the evolution of the cosmic SFR up to $z \sim 2$. This is the maximum that narrow-band surveys can probe from the ground as $\text{H}\alpha$ falls into the mid-IR for higher redshifts, which is then blocked by water vapor and carbon diox-

ide in the atmosphere. To probe to higher- z using the same narrow-band technique would require another emission line. The other major emission lines associated with star-forming galaxies are $\text{H}\beta$ 4861, [OIII]4959, [OIII]5007, and [OII]3727 which can be probed up to $z \sim 3$ for $\text{H}\beta+[\text{OIII}]$ and up to $z \sim 5$ for [OII].

In the past decade, several $\text{H}\beta$, [OIII], and [OII] studies have been carried out (e.g., Hammer et al. 1997; Hogg et al. 1998; Gallego et al. 2002; Hicks et al. 2002; Teplitz et al. 2003; Ly et al. 2007; Takahashi et al. 2007; Bayliss et al. 2011, 2012; Sobral et al. 2012; Ciardullo et al. 2013), the majority of which had small sample sizes and, hence, suffered from cosmic variance biases. The majority observed up to $z \sim 1$, while only the works of Bayliss et al. (2011) and Bayliss et al. (2012) measured the [OII] SFR densities at $z \sim 2$ and $z \sim 4.6$, respectively. Both these works used small samples, with the $z \sim 4.6$ measurement having a sample size of only 3 [OII] emitters, greatly limiting any conclusion.

This paper presents, for the first time, the luminosity functions of $\text{H}\beta+[\text{OIII}]^1$ and [OII] emitters up to $z \sim 5$ using the reliable selection techniques of Sobral et al. (2009, 2012, 2013) on the combined COSMOS and UDS narrow-band publicly available catalogs² of HiZELS. The sample probes comoving volumes of up to $\sim 1 \times 10^6 \text{ Mpc}^3$, which greatly reduces the effects of cosmic variance. This is also the largest sample of $\text{H}\beta+[\text{OIII}]$ and [OII] emission line galaxies up to $z \sim 5$ to date in the literature and is used to effectively and robustly probe the evolution of the cosmic SFR density.

This paper is organized as follows: in Section 2, we outline the photometric and spectroscopic data sets that we use and the methodology utilized to effectively select $\text{H}\beta+[\text{OIII}]$ and [OII] emitters. In Section 3, we outline our volume calculations and the completeness and filter profile corrections. Also in Section 3 are the results of the luminosity functions. In Section 4, we present the results and discuss our cosmic star-formation rate densities and the evolution of the stellar mass density based on [OII] emitters. Section 5 outlines the conclusion of this work and is followed by appendix A, which presents our color-color selection criteria, and appendix B, which presents our binned luminosity function data points, and appendix C, which presents our SFR density compilation.

Throughout this paper, we assume ΛCDM cosmology with $H_0 = 70 \text{ km s}^{-1} \text{ Mpc}^{-1}$, $\Omega_m = 0.3$, and $\Omega_{\Lambda} = 0.7$ with all magnitudes presented as AB and the initial mass function is assumed to be a Salpeter IMF.

¹ Because the $\text{H}\beta$ and [OIII] emission lines are close to each other, photo- z and color-color selections can not distinguish between them. The best way to fully differentiate the two is via spectroscopy. Based on line ratio studies, we can argue that most of the emitters will be [OIII] emitters, but to ensure we are not biasing our measurements based on such assumptions, we present the results as the combined measurement of $\text{H}\beta+[\text{OIII}]$.

² The narrow-band catalogs are available on VizieR and are from Sobral et al. (2013).

Table 1. A list of the narrow-band filters used (Sobral et al. 2013), along with the central wavelength (μm) and the FWHM (\AA) of each filter. Included is the expected redshift of each emission line within the range of the FWHM of the filter and the comoving volume that is observed.

| Filter | λ_{obs} (μm) | FWHM (\AA) | $H\beta+[OIII]5007$ | | $[OII]3727$ | |
|--------|---|--------------------------|---------------------|---|-----------------|---|
| | | | z | Volume ($10^5 \text{ Mpc}^3 \text{ deg}^{-2}$) | z | Volume ($10^5 \text{ Mpc}^3 \text{ deg}^{-2}$) |
| NB921 | 0.9196 | 132 | 0.84 ± 0.01 | 1.79 | 1.47 ± 0.02 | 3.75 |
| NBJ | 1.211 | 150 | 1.42 ± 0.01 | 3.11 | 2.25 ± 0.02 | 4.83 |
| NBH | 1.617 | 211 | 2.23 ± 0.02 | 5.05 | 3.34 ± 0.03 | 6.53 |
| NBK | 2.121 | 210 | 3.24 ± 0.02 | 4.87 | 4.69 ± 0.03 | 5.68 |

2 DATA

2.1 Selection Catalogs

Our data consist of narrow-band and broad-band photometric data of the UDS and COSMOS fields and spectroscopic follow-ups that are described in section 2.4. The catalogs that are described below are taken from Sobral et al. (2013) and are publicly available.

The narrow-band catalogs are from the High- z Emission Line Survey (HiZELS, Geach et al. 2008; Sobral et al. 2009, 2012, 2013). This project utilizes the narrow-band J , H , and K filters of the Wide Field CAMera (WFCAM) on the United Kingdom Infrared Telescope (UKIRT) and the NB921 filter of the Suprime-Cam on the Subaru Telescope. Previous uses of this data focused primarily on $\text{H}\alpha$ emitting galaxies and their properties (e.g., Garn et al. 2010; Geach et al. 2012; Sobral et al. 2010, 2011, 2013; Stott et al. 2013a,b; Swinbank et al. 2012a,b; Darvish et al. 2014), but HiZELS is able to pickup more than just this emission line as it can detect any line above the flux limit. In this paper, we focus on the $H\beta+[OIII]$ and $[OII]$ emitting galaxies found by HiZELS. The broad-band catalogs are from the Cosmological Evolution Survey (COSMOS; Scoville et al. 2007) and the DR8 release of the Subaru-*XMM*-UKIDSS Ultra Deep Survey (UDS; Lawrence et al. 2007) catalog.³

2.2 Narrow-Band Selection of Potential Emitters

In this subsection, we will review the methodology of selecting potential emitters followed by Sobral et al. (2013). We refer the reader to this paper for a detailed overview.

Potential emitters were selected by their color excess in terms of the parameter Σ (Bunker et al. 1995; Sobral et al. 2012), which quantifies the significance of the excess of a source with respect to the random scatter expected for a source to have a color excess > 0 in terms of their narrow-band magnitudes:

$$\Sigma = \frac{1 - 10^{-0.4(\text{BB}-\text{NB})}}{10^{-0.4(\text{ZP}-\text{NB})} \sqrt{\pi r_{\text{ap}}^2 (\sigma_{\text{NB}}^2 - \sigma_{\text{BB}}^2)}} \quad (1)$$

where BB and NB are the broad-band and narrow-band

³ We refer the reader to the respective papers for further details on the creation of these catalogs. We also refer the reader to the UKIDSS and COSMOS websites for further information of the multi-wavelength photometric and spectroscopic data sets. (COSMOS: <http://irsa.ipac.caltech.edu/data/COSMOS>; UDS: <http://www.ukidss.org>)

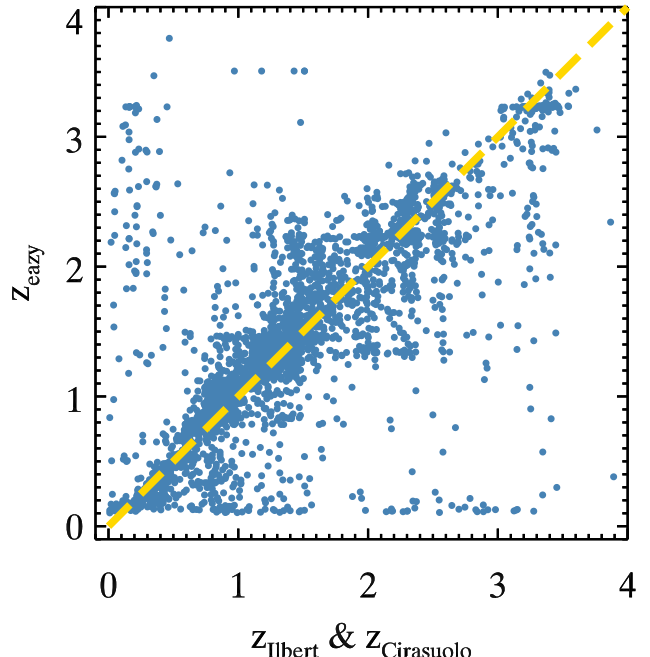


Figure 1. The comparison between the photo- z measurements from EaZY and from Ilbert et al. (2009) (COSMOS) and Cirasuolo et al. (2007) (UDS) for all narrow-band excess sources. The *gold line* going across is the 1:1 relation. As expected, we find that the majority of our emitters follow this linear relation resulting in a reasonable agreement with the measurements found in the initial catalogs. The scatter is mainly caused by the introduction of the tightly constrained NB photometry that forces the SED to match with the detected emission lines. We find a $\Delta z / (1 + z_{\text{spec}}) = 0.037$.

magnitudes, respectively, r_{ap} is the aperture radius in pixels, and σ_{BB} and σ_{NB} are the rms per pixel for the broad-band and narrow-band, respectively (see e.g. Sobral et al. 2012, 2013).

Emitters are selected on the basis that they have $\Sigma > 3$ and a rest-frame equivalent width $\text{EW}_0 > 25 \text{ \AA}$. The second condition ensures that we select sources with a significant color excess for bright narrow-band magnitudes (see fig. 3 of Sobral et al. 2013).

2.3 Photo- z Measurements

We use the COSMOS and UDS catalogs with photo- z measurements from Ilbert et al. (2009) and Cirasuolo et al. (2007) for COSMOS and UDS, respectively. The UDS cat-

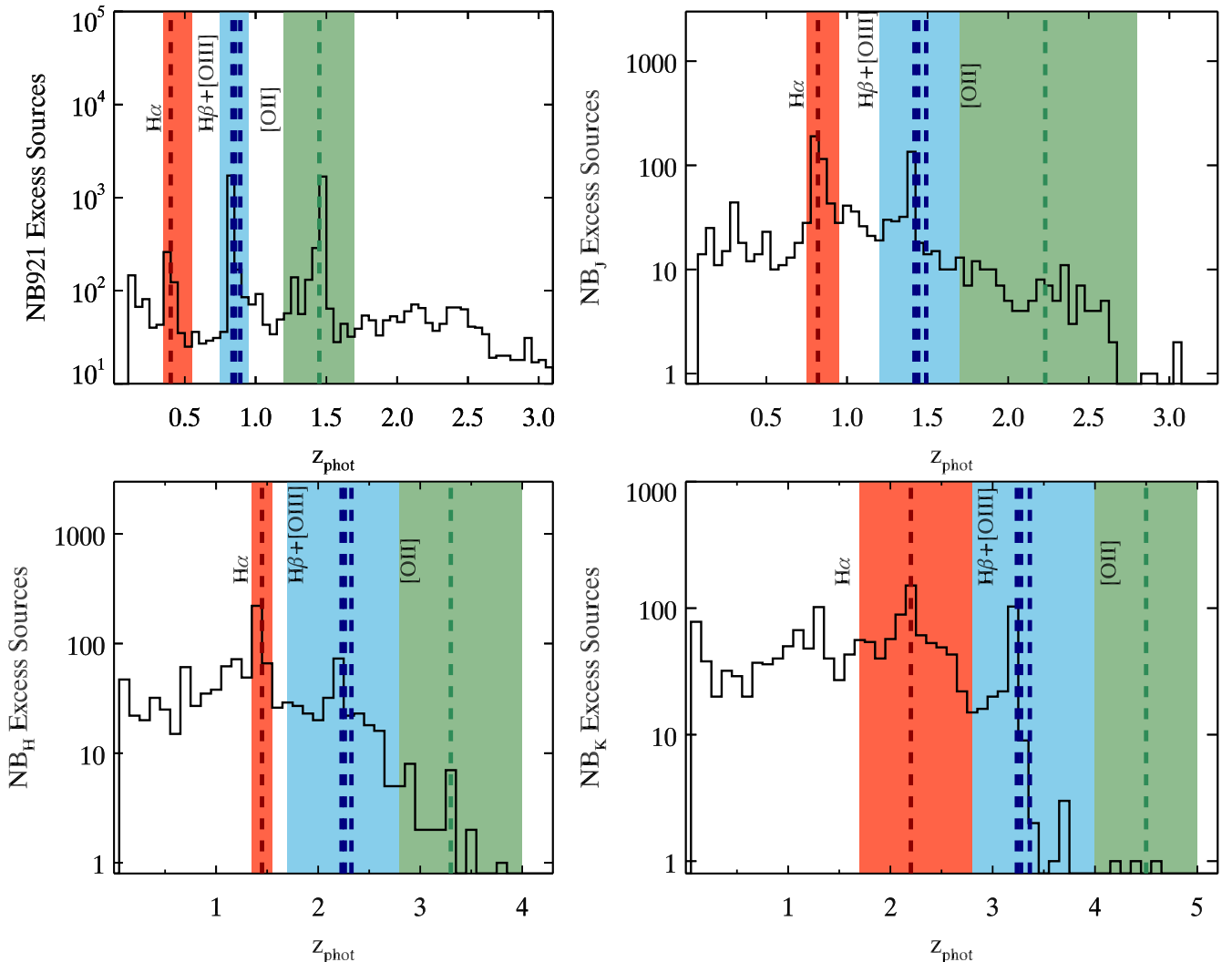


Figure 2. Log-scale photometric redshift distributions of the emitters selected in NB921 (upper left), NB_J (upper right), NB_H (lower left), and NB_K (lower right). Each main peak is associated with a strong emission line, specifically H α , H β +[OIII], and [OII]. The dashed red line is the expected redshift of H α emitters. The dashed blue lines are the expected redshifts for H β +[OIII] emitters corresponding to H β 4861, [OIII]4959, and [OIII]5007. It is clear then that differentiating these lines, even in narrow-band surveys, is quite difficult due to their close proximity to each other. Lastly, the dashed green line is the expected redshift of [OII] emitters. Highlighted in the corresponding, but lighter colors, are the photo- z selection regions. The H α selection region is from Sobral et al. (2013). The photo- z distributions are from our photo- z calculations using EaZY for the COSMOS and UDS fields.

alog had more than $> 60\%$ of their sources without photometric redshifts. This resulted in many of our emitters not being selected via the photometric redshift selection method. Although the color-color selection is effective alone in selecting H β +[OIII] and [OII] emitters (see below for discussion), we wish to have emitters selected by two independent methods to ensure completeness. Therefore, we measured the photometric redshifts for all of the UDS and COSMOS narrow-band excess sources, using EaZY (Brammer, van Dokkum & Coppi 2008) to ensure that (1) the majority of the UDS catalog had reliable photometric redshifts, and (2) that both COSMOS and UDS had their redshifts determined by the same code, models, and assumptions. We use the *UBVgRizJK* bands as well as the *GALEX* FUV and NUV bands, the *Spitzer* IRAC 3.6 μ m to 8.0 μ m, and the narrow-band filters to measure the red-

shifts for COSMOS. For UDS, we use the *UBVRizYJHK*, the *Spitzer* IRAC 3.6 μ m to 8.0 μ m, and the narrow-band filters. The benefit of using the narrow-band filters in measuring the redshifts is that these filters specifically capture emission-lines which are inherent in the SEDs. We also used the Pegase13 spectral library in determining the redshifts. Figure 1 shows the comparison between the measurements in the original catalogs and those that we measured with EaZY. Figure 1 only shows emitters that did have previous photo- z measurements in the UDS and COSMOS catalogs. Figure 2 shows the redshift distribution for all emitters in the catalogs. We find that, overall, our measurements are in agreement with those measured by Ilbert et al. (2009) and Cirasuolo et al. (2007) with median errors of $\Delta z / (1 + z_{spec}) = 0.037$ for the whole sample (0.034 and 0.047 for COSMOS and UDS, respectively).

Table 2. The number of emitters selected based on color-color, photo- z , spec- z , and dual/multi-emitters. We also include the total number of emitters found. It should be noted that an emitter can be selected by more than just one selection, such that by tallying up the number of emitters per column will result in a number larger than the number in the column that shows the total number of emitters.

| Emission Line | Band | z | Color-Color | Photo- z | Spec- z | Dual/Multi-Emitter | Total |
|-----------------------------------|-------|------|-------------|------------|-----------|--------------------|-------|
| $H\beta+[OIII]$ | | | | | | | |
| | NB921 | 0.84 | 2005 | 1638 | 213 | 4 | 2676 |
| | NBJ | 1.42 | 212 | 285 | 15 | 0 | 303 |
| | NBH | 2.23 | 225 | 268 | 3 | 1 | 329 |
| | NBK | 3.24 | 142 | 175 | 1 | 0 | 176 |
| $[OII]$ | | | | | | | |
| | NB921 | 1.47 | 3012 | 2121 | 97 | 67 | 3138 |
| | NBJ | 2.25 | 77 | 124 | 0 | 1 | 125 |
| | NBH | 3.34 | 16 | 27 | 1 | 0 | 28 |
| | NBK | 4.69 | 10 | 1 | 0 | 0 | 10 |

2.4 Spectroscopic Redshifts

We make use of the vast array of spectroscopic observations from the literature, which greatly enhances the completeness and reliability of our measurements. In the COSMOS catalog, spectroscopic measurements are drawn from various studies as listed on the COSMOS website, as well as the zCOSMOS measurements from Lilly et al. (2007). The UDS catalog also includes measurements from various publications that are highlighted on the UKIDSS UKIRT website, including the UDSz survey (Bradshaw et al. 2013; McLure et al. 2013). We also include FMOS measurements from Stott et al. (2013a), DEIMOS & MOSFIRE measurements from Nayyeri et al., in prep, PRIMUS measurements from Coil et al. (2011), and VIPERS measurements from Garilli et al. (2014). In total, we have 1269 emitters that have spectroscopic redshifts with 661, 350, 177, and 81 emitters in NB921, NBJ, NBH, and NBK, respectively. This allows us to enhance the completeness of our measurements and to test our photo- z and color-color selections.

2.5 Selection of $H\beta+[OIII]$ and $[OII]$ Emitters

The selection of potential $H\beta+[OIII]$ and $[OII]$ emitters is done by a combination of three different methods: (1) photometric redshift; (2) color-color; and (3) spectroscopic redshift. In this section, we will present the general selection criteria that we used to select our sample. For more detailed information about the specific selection cuts applied in each case, we refer the reader to appendix A.

As shown in figure 2, the local peaks in the photometric redshift distributions are located around the expected redshifts for $H\beta+[OIII]$ and $[OII]$ emitters. This signifies that we have many $H\beta+[OIII]$ and $[OII]$ emitters in our sample. We select our emitter candidates by defining a range in the distribution of z_{phot} that is centered on the expected redshift of the emission line, which is aligned with the peaks in figure 2. In most cases, the number of $H\alpha$ emitters are the largest, followed by $H\beta+[OIII]$ and $[OII]$. In NB921 (figure 2), $H\beta+[OIII]$ and $[OII]$ lines are the strongest, respectively, as these redshifts are near the peak of the cosmic star-formation history and also probe a much larger cosmic volume that $H\alpha$. Other populations of emission lines are

found, such as Paschen series lines, HeI, and $[SIII]$ (figure 2).

Color-color selections are also applied for each redshift. The selection criteria used for $z \sim 1 - 3$ are from Sobral et al. (2013) as these are in perfect agreement with our large spectroscopic sample, while the criteria used for the $H\beta+[OIII]$ and $[OII]$ at $z = 3.3$ and $[OII]$ at $z = 4.5$ are based on the dropout color-color selection known as the Lyman break technique (Dickinson 1998; Stark et al. 2009). For some redshifts, we use more than one color-color selection to reduce the contaminations from lower and higher- z sources. All color-color selection definitions are found in table A1.

Whenever available, we select sources based on their spectroscopic redshifts. Any source that is spectroscopically confirmed to have a line besides the one of interest is omitted. By including spectroscopically confirmed sources, we increase the completeness of our sample. We also note that we use all our spectroscopic redshifts to confirm the robustness and completeness of our photo- z and color-color selections.

There are cases where we find that the results of the three different selection methods are in conflict. To alleviate the issue, we prioritize the selection methods as such: 1) spectroscopic redshifts, 2) photometric redshifts, and 3) color-color. If the emitter has a spectroscopic redshift, then it is selected based only on that. If it doesn't, then we select it based on its photometric redshift. Lastly, if the emitter has a photometric redshift but is not within the range of being selected as $H\alpha$ (see photo- z selection criteria in Sobral et al. 2013), $H\beta+[OIII]$, or $[OII]$ or if the emitter does not have photo- z measurements, then it is selected based on the color-color criterion. In most cases, we find that emitters with photo- z within the redshift selection range are also found within the color-color selection area. In such cases, the emitters are selected based on both selection methods.

Also in the selection process is selecting dual/multi-emitters. For some sources that are selected as emitters with some emission line, there also exists another emission line in another band. For example, an emitter that is selected in NBJ as an $H\beta+[OIII]$ emitter ($z = 1.47$) can also be selected in NB921 as an $[OII]$ emitter if observed in that narrow-band. Sobral et al. (2012) used this same technique in a double-blind study to find $[OII]$ emitters in NB921 by

using selected $\text{H}\alpha$ emitters in NBH as a proxy. The benefit to this technique is that it confirms emitters if they are selected in at least two bands; corresponding to getting a redshift out of two emission lines.

One major source of contamination that we may have is having selected a source as an [OII] emitter when it is an $\text{H}\beta+[\text{OIII}]$ emitter and vice versa. Also, there are situations where a source is selected as one of the emitters of interest, but also falls into the color-color selection for another emission line, or even $\text{H}\alpha$ (as these color-color selections were used by Sobral et al. (2009, 2012, 2013) to find such emitters). To overcome this degeneracy, we look at the photo- z distributions shown in figure 2 as a probability distribution to assign the emission line based on the most probable line in the sample. In all cases, except for NB921, $\text{H}\alpha$ is the most probable line. For NB921, $\text{H}\beta+[\text{OIII}]$ is the most probable.

Another source of contamination is from misidentified lines. From the wealth of spectra that we have, the majority of misidentified lines are $\text{H}\alpha$. Further details on the types of misidentified lines can be found in appendix A. Our total sample size is outlined in table 2.

3 LUMINOSITY FUNCTIONS AND EVOLUTION

We use the traditional V_{max} estimator to create our binned data. The binned data is defined such that:

$$\phi(L_j) = \frac{1}{\Delta \log L_{b,j}} \sum_{\log L_{c,j} - \Delta \log L_{b,j}/2}^N \frac{1}{C(L_i)V_{max,i}} \quad (2)$$

where L_j is the j^{th} luminosity bin, $\Delta \log L_{b,j}$ is the bin-size, $\log L_{c,j}$ is the central luminosity of the j^{th} bin, $C(L_i)$ being the completeness of the i^{th} source described in section 3.1, and $V_{max,i}$ being the volume for which that source may be detected as described in section 3.2.

3.1 Line Completeness

To assess the completeness, we follow the methodology proposed in Sobral et al. (2012, 2013). We start with the full catalog and extract sources which did not make our emitter selection. For each source, we input a line flux starting at $10^{-18} \text{ erg s}^{-1} \text{ cm}^{-2}$ and increase it in small increments. For each line flux, we apply our Σ and EW criteria. We then apply our color-color selections and compare the number of sources recovered to the total number of sources in the catalog. Figure 3 shows the average completeness determined for our $\text{H}\beta+[\text{OIII}]$ and [OII] sources in the different narrow bands. The advantage of this technique is that we are not limiting our determination of the completeness to a certain model, but actually using the observed data itself to get the completeness correction.

There are some important points to be noted. First, these simulations are run separately per image. This is because the depths of each image are not the same and thus can not be used together all at once to determine the completeness correction. Secondly, we apply an uncertainty of 20% of the completeness correction to the other uncertainties in quadrature in order to take into account the errors associated with this method of determining the corrections.

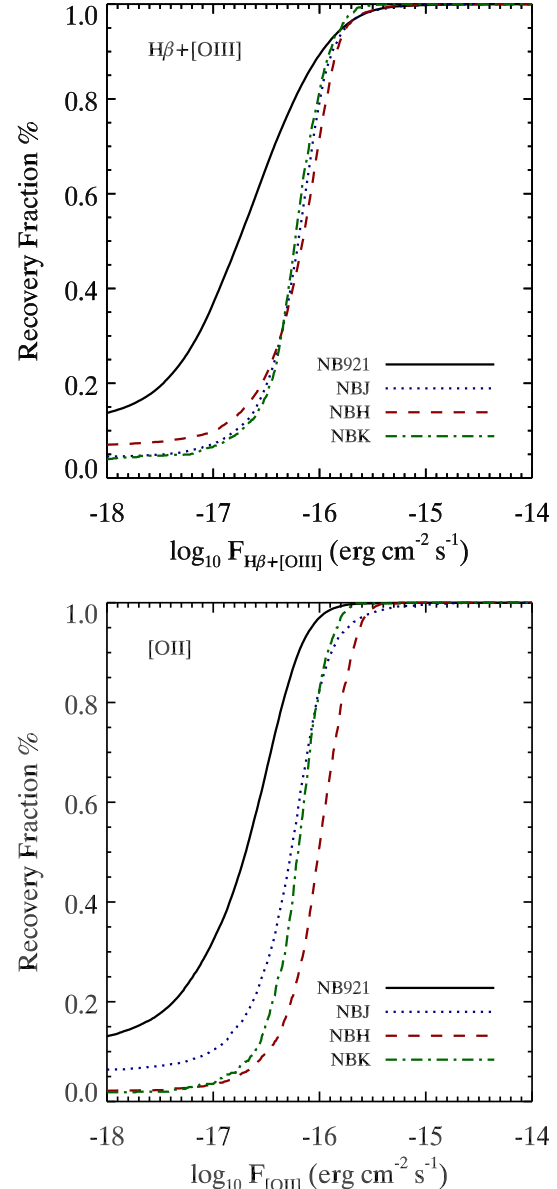


Figure 3. Average line completeness for the entire sample per band. Note that the completeness does vary between the COSMOS and UDS fields, as well as from image-to-image within each field. This is because each image has a different depth. We compute the completeness based on each image to account for this discrepancy.

3.2 Volumes & Filter Profile Correction

We calculate the volumes assuming a top-hat filter that has the same range as the FWHM of the actual filter. We report the probed comoving volume per square degree in table 1. The volumes for each log-luminosity bins in the luminosity functions are reported in tables B1 and B2 for $\text{H}\beta+[\text{OIII}]$ and [OII], respectively.

Although a top-hat filter makes our calculations easy, it is not a true representation of the throughput of the filter, which requires us to apply a filter profile correction. There are two main effects that the filter profile correction takes

into account. The first is the *flux loss due to emitters that are close to the edge of the filter's FWHM*. Bright emitters at the wings will have a significant flux loss (close to 40%; depends on the filter) and would be considered as a faint source. This gives an overall bias in our sample population of faint sources and a lack of bright sources. The second effect is the *volumes are corrected for the bright sources*. Any faint source that is close to the wings of the filter will most likely not be in our sample, but bright sources will be detected as faint emitters. This then implies that our bright emitters cover a wider range of the filter, meaning a wider range in redshift, and, therefore, a larger volume.

We use the method proposed in Sobral et al. (2009, 2012, 2013). We correct for the filter by creating a mock sample of 10^5 fake emitters based on the luminosity function with the assumption of a top-hat filter. Random redshifts are assigned to each source and in a range covering the full filter profile, but not large enough that evolutionary effects of the luminosity function and cosmological structure biases the results. We assume a uniform redshift distribution. This mock sample will have the same distribution as the inputted top-hat luminosity function which we define as ϕ_{TH} . We then make a second mock sample with the same top-hat luminosity function but now apply the actual filter. This is done by:

$$L_{corr} = \frac{\int_{z_1}^{z_2} L_{in}(z) T(z) dz}{\int_{z_1}^{z_2} T(z) dz} \quad (3)$$

where $T(z)$ is the filter-response function in terms of redshift and $L_{in}(z)$ is the luminosity of the emitter which is defined as $L_{in}(z) = L \delta(z_{rand} - z_{filter})$, where z_{rand} is the randomly assigned redshift and z_{filter} is the matching redshift of the filter. This results in the loss of sources as some sources will have a redshift outside the range of the filter's FWHM. The luminosity function from this population is defined as ϕ_{Filter} and is compared to ϕ_{TH} in order to get the filter profile correction factor. The result shows that the bright sources are underestimated as expected, which changes the shape of the final luminosity function slightly. Specifically, it decreases the faint-end slope and increases the L_* and ϕ_* slightly.

3.3 Luminosity Function Fitting

There are several different functions that have been proposed in the literature to describe the observed luminosity function of the Universe (see Johnston 2011 for an in-depth review). We adopt the most-widely accepted Schechter function to fit the observed luminosity function. The Schechter function is defined in its log-form as:

$$\Phi(L) dL = \phi_* \ln 10 \left(\frac{L}{L_*} \right)^{1+\alpha} e^{-(L/L_*)} d \log_{10} L \quad (4)$$

where ϕ_* is the normalization of the luminosity function, L_* is the characteristic luminosity, and α is the faint-end slope.

We fit each luminosity function using the MPFIT fitting routine (Markwardt 2009), which utilizes the Levenberg-Marquardt least-squares minimization technique to find the best-fit for a given function. For each fit, we take the best-fit values as our fitted parameters. For the 1σ errors, we run a Monte Carlo simulation, similar to that of Ly et al.

(2011). The simulation starts by randomly selecting a random number that is drawn from a normal distribution that will perturb each data point, $\Phi(L)$, in the luminosity function within the 1σ error bars. We also vary the bin size and center of the bin by perturbing the original bin size and bin center by a uniform distribution. The fit is then run again and these steps are repeated for each iteration. A total of 10^5 iterations are done to get a probability distribution of the best-fit values from where the 1σ error bars are then calculated.

Our best-fit values are shown in table 3. We keep α fixed to a constant value of -1.5 and -1.3 for $H\beta+[OIII]$ and $[OII]$, respectively, as we are not able to fully constrain the faint-end. These values are drawn from looking at past work from previous narrow-band studies in order for our results to be comparable. The drawback to this is that we are using low- z measurements of α as a proxy for the high- z universe, which can be an incorrect assumption. Low- z studies, such as Colbert et al. (2013); Ly et al. (2007) and Pirzkal et al. (2013) for $H\beta+[OIII]$ and Ly et al. (2007); Ciardullo et al. (2013); Takahashi et al. (2007); Bayliss et al. (2011) and Sobral et al. (2012) for $[OII]$, have shown that the faint-end slope doesn't evolve up to $z \sim 1.5$, while $H\alpha$ surveys such as Sobral et al. (2013, 2014) have shown no evolution in the faint-end slope up to $z \sim 2.23$. Furthermore, UV studies (e.g., Oesch et al. 2010; Smit et al. 2012), have shown no evolution up to $z \sim 6 - 7$. Based on these results, we keep α fixed as we constrain the bright-end rather than the faint-end.

Lastly, the LF results are not corrected for dust extinction, except when measuring the star-formation rate densities. This is because many studies in the literature use very different extinction diagnostics, such that it becomes difficult to compare various studies. Furthermore, our knowledge regarding the role of dust in the high- z universe, especially for $H\beta+[OIII]$ and $[OII]$ emission line galaxies is poor at best and will require future detailed investigations. To simplify the use of our LFs by others in future studies, we present all the LF parameter results as uncorrected for dust and AGN contribution. When discussing the SFRDs in section 4, we will include the results with and without dust and AGN corrections.

3.4 $H\beta+[OIII]$ Luminosity Function $z \sim 0.8, 1.5, 2.2$, and 3.3

We present here the results of the fitted Schechter function to the $H\beta+[OIII]$ observed luminosity function out to $z \sim 3.3$. This is the highest redshift determination of the $H\beta+[OIII]$ LFs currently to date and is the first time that the luminosity function has been constrained out to these redshifts. We present the results in figure 4. From $z \sim 0.8$ to 3.3 , we see a clear evolution in the shape of the LFs (figure 4, left). We also show on figure 4 the evolution of ϕ_* and L_* with α fixed to -1.6 . It should be noted that there is a degeneracy between the fitted Schechter parameters, as shown in figure 7. This needs to be borne in mind when interpreting the evolution of any single parameter, although figure 7 indicates that our results are relatively robust. Based on our results, we find that ϕ_* has been decreasing from $z \sim 0.8$ to 2.2 and then flattens by $z \sim 3.3$. The opposite trend is

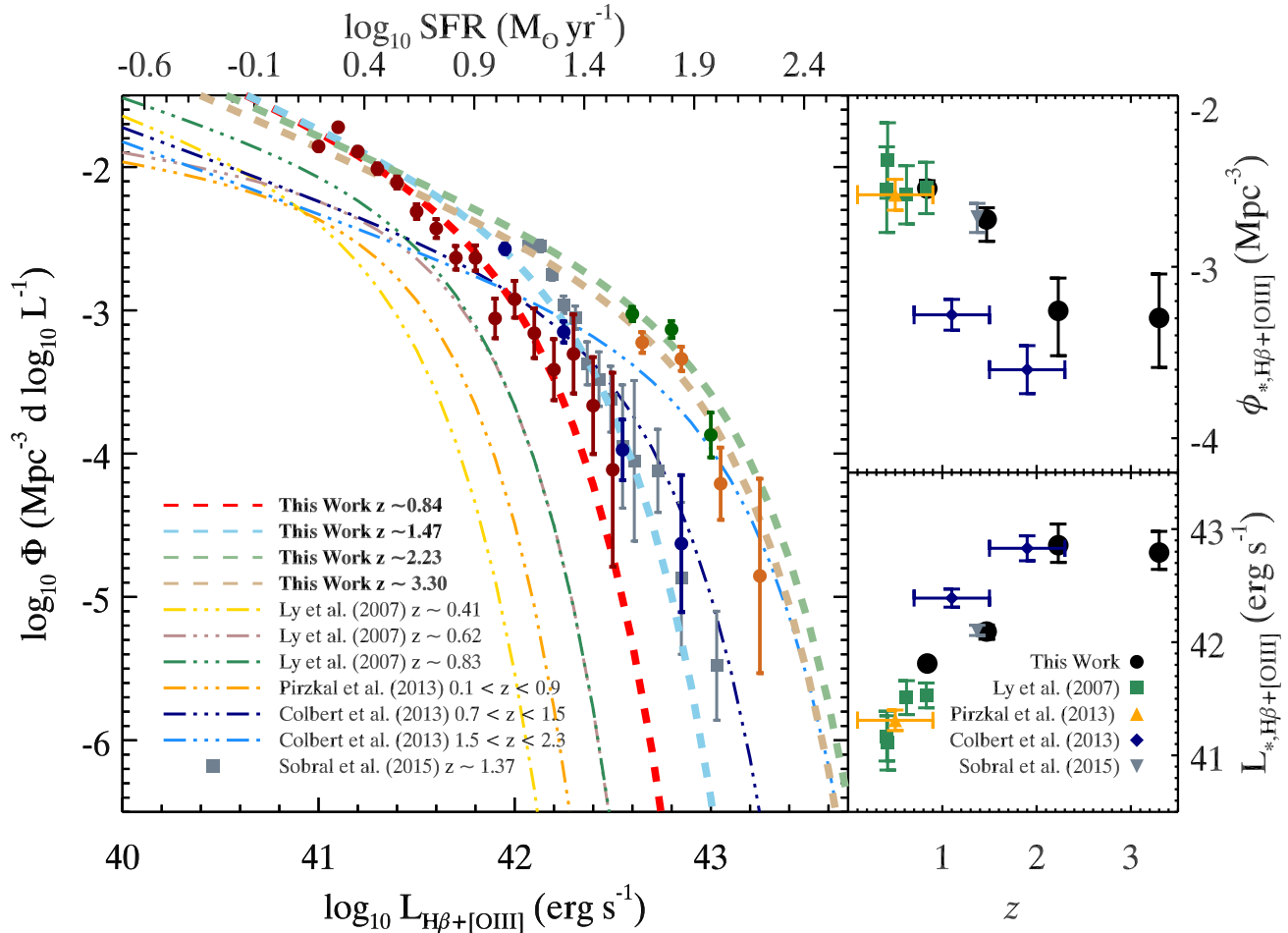


Figure 4. *Left:* Presented are our H β +[OIII] Luminosity Functions along with LFs from the literature. The darker data points are color coded to match the lighter LF fit (*dashed lines*). There is a clear evolution in the LFs up to $z \sim 3$. We find that our $z = 1.47$ and 2.23 LFs are in reasonable agreement with the [OIII] grism spectroscopy study of Colbert et al. (2013) at the bright-end, suggesting that we are selecting a reliable sample of [OIII] emitters. The major difference between our $z = 0.84$ and the $z = 0.83$ LF of Ly et al. (2007) is probably due to sample size biases. Our sample is much larger, hence we are able to populate our brightest bins, causing a shift in L_* to higher luminosities. *Top Right:* The evolution of ϕ_* from the H β +[OIII] luminosity function. A clear evolution is seen with ϕ_* dropping from $z = 0$ to $z \sim 2$ and then flattening to $z \sim 3$. This same evolution is seen by UV LF studies (see Oesch et al. 2010 for details). *Bottom Right:* The evolution of L_* from the H β +[OIII] luminosity function. The evolution is strong as L_* rises up to $z \sim 2$ and flattens by $z \sim 3$.

seen in L_* where it is increasing from $z \sim 0.8$ to $z \sim 2.2$ and flattens by $z \sim 3.3$.

Our results show a clear evolution in the luminosity function and are consistent with the same evolution seen in the results from the literature (Ly et al. 2007; Pirzkal et al. 2013; Colbert et al. 2013; Sobral et al. 2015). We report our LF parameters in table 3. We find that our $z \sim 1.47$ and 2.23 LF agrees well with the LFs of Colbert et al. (2013) in the bright-end, but diverges at the faint-end. This matches with our discussion in the section below (see section 3.4.1) where we predict the bright-end to be dominated by [OIII] emitters. The Colbert et al. (2013) study was part of the *HST* WISP program, covering 29 fields (0.036 deg^2) in search of H α , [OIII], and [OII] emission line galaxies using WFC3 grism spectroscopy. Because this was a spectroscopic study and the fact that our LF matches (in the bright-end) with that of Colbert et al. (2013) gives us confirmation that we are picking up the [OIII] emitters in our sample. The rise in the

faint-end can then be attributed to the H β emitters in our sample.

In comparison to Ly et al. (2007), we see a clear deviation of the fits between our $z \sim 0.8$ and their $z \sim 0.83$ in the bright-end while we are in agreement in the faint-end. The study was based on deep optical imaging of the Subaru Deep Field (SDF) using the Suprime-Cam on the 8.2 m Subaru Telescope and was complemented with Subaru DEIMOS and Keck DEIMOS spectroscopy. The deviation could be due to biases from sample sizes such that our sample consists of more brighter emitters to populate the bright-end, hence shifting L_* higher. In comparison to Sobral et al. (2015), for which this work was done in unison with, we find perfect agreement but our sample probes deeper by 0.4 dex.

Figure 4 shows the evolution of L_* along with the results from other studies. There is a strong trend in which L_* is increasing from $z = 0 - 2.23$ and then flattens. This

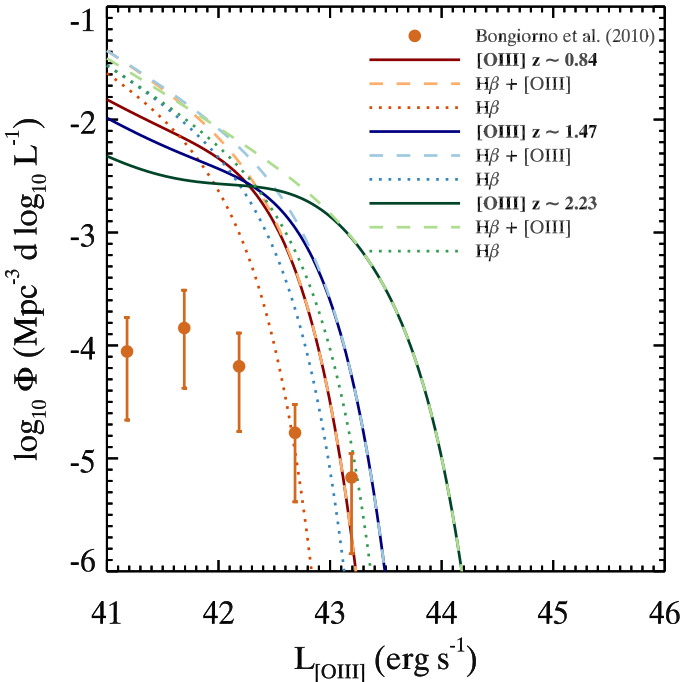


Figure 5. Shown is the predicted [OIII] LFs from $z \sim 0.8$ to 2.2 and compared to the $z \sim 0.71$ zCOSMOS Type-2 AGN LF of Bongiorno et al. (2010). The $H\beta$ LFs are made by simply taking the $H\alpha$ LFs of Sobral et al. (2013) and assuming a fixed $H\beta/H\alpha$ ratio to convert them. We find that our $z \sim 0.84$ LF is [OIII]-dominated at the bright-end. Also, the level of AGN contribution is very little, except for $L_{[OIII]} > 43.0 \text{ erg s}^{-1}$.

trend is supported by Ly et al. (2007), Pirzkal et al. (2013), Colbert et al. (2013), and Sobral et al. (2015).

For the normalization of the LF, we see an evolution (figure 4) such that ϕ_* drops as redshift increase up to $z \sim 2$ and flattens after $z \sim 3$. This is consistent with the collection of UV LFs (i.e., Oesch et al. 2010), while our determination is based on a reliable $H\beta+[OIII]$ sample.

3.4.1 Predicting the [OIII] LF and AGN contribution

The results highlighted above are for the $H\beta$ and [OIII] emitters combined as one sample since we can not separate the two types of emitters based on photometry. For this, we need to conduct spectroscopic follow-ups to properly segregate the emitters. We attempted to separate the sample by using the $H\alpha$ LF of Sobral et al. (2013). The advantage of using the LFs of Sobral et al. (2013) is that it is fully compatible since we are both using the same data set and methodology. We start by first removing the $A_{H\alpha} = 1.0 \text{ mag}$ dust correction, then apply an $H\beta/H\alpha = 0.35$ line ratio from Osterbrock & Ferland (2006) to get the observed $H\beta$ LF. We then applied $A_{H\beta} = 1.38 \text{ mag}$ (based on Calzetti et al. (2000); assuming $A_{H\alpha} = 1.0 \text{ mag}$) to the LFs and dust-corrected our $H\beta+[OIII]$ LFs using $A_{H\beta+[OIII]} = 1.35$ (see section 4.3.2 for details). The next step was subtracting our $H\beta+[OIII]$ LFs from the predicted $H\beta$ LFs to get the predicted luminosity function for [OIII]5007 emitters. The results are shown in figure 5.

We find that the [OIII] emitters in our sample completely dominate the $H\beta+[OIII]$ LFs. At the faint-end, we

find that the $H\beta$ emitters dominate. This is expected as the theoretical [OIII]/ $H\beta$ line ratio is ~ 3 (for $Z = 0.0004$; Osterbrock & Ferland 2006), which would segregate our sample such that the bright-end will be populated by [OIII] emitters and the faint-end with $H\beta$ emitters. We also do find an interesting feature where the drop in the normalization of the [OIII] LF increases as a function of redshift. This can be explained in several ways. One possibility is that the number of [OIII]4959 emitters is increasing as a function of redshift. The predicted [OIII] LF that we present here is for the 5007Å line as this is the dominate of the [OIII] emission lines. Other possibilities include an evolution of metallicity and an increase in $H\beta$ emitters as a function of redshift.

We also attempted to compare the $z \sim 0.8$ [OIII] LF with the zCOSMOS AGN Type-2 LF of Bongiorno et al. (2010) to qualitatively assess the contribution of AGNs. The Type-2 AGN is the best candidate that could contaminate our sample as they have a continuum that is similar to normal star-forming galaxies and they photo-ionize the same cold gas that is photo-ionized by hot massive stars. We find that we are in agreement *only* for the brightest luminosity bin of Bongiorno et al. (2010) ($L_{[OIII]} \sim 43 \text{ erg s}^{-1}$), but in disagreement for the lower luminosity bins. This implies that our brightest [OIII] emitters are primarily AGNs, but the fainter emitters are a combination of star-forming galaxies and AGNs, with the star-forming galaxies being the most dominant. Future spectroscopic follow-ups of our sample would allow us to properly study the evolution of AGNs in the Universe.

3.5 [OII] Luminosity Function $z = 1.47, 2.23, 3.3$, and 4.7

We present here the results of the [OII] luminosity function and the Schechter fit out to $z \sim 5$. The results are highlighted in figure 6. We see a clear evolution of the LF with redshift, with a large increase in the characteristic luminosity with redshift. The right-hand panels of figure 6 show the evolution of the fitted ϕ_* and L_* parameters, and figure 7 shows the degeneracy between the fitted values.

Included on figure 6 are data from the literature that range from $z = 0 - 2.2$ (Bayliss et al. 2011; Ciardullo et al. 2013; Ly et al. 2007; Takahashi et al. 2007; Sobral et al. 2012, 2015). We find that our $z = 2.23$ binned LF data is in agreement with the CF-HiZELS result of Sobral et al. (2015). Because their sample size is ~ 4 times larger than our measurement, we have combined their LF data points with ours. The main effect is our measurement extends the combined LF 0.2 dex fainter. We note that the LFs of Sobral et al. (2015) are directly compatible with our LFs as our study follows the same methodology. In fact, the Sobral et al. (2015) is specific to the NBJ determined LFs while this study focuses on the evolution and extension of the LFs out to $z \sim 5$.

Our $z = 1.47$ measurements are in perfect agreement with Sobral et al. (2012) and close to agreement with Ly et al. (2007). We note that for Ly et al. (2007) the faint-end was measured to be $\alpha = -0.78 \pm 0.13$ and -0.9 ± 0.2 for Sobral et al. (2012) while we keep our faint-end slope fixed to -1.3 for all LFs. As seen in figure 6, we find that we are not probing deep enough to fully see the turn in the LF for $L_{[OII]} < 41 \text{ erg s}^{-1}$ as found by Ly et al. (2007)

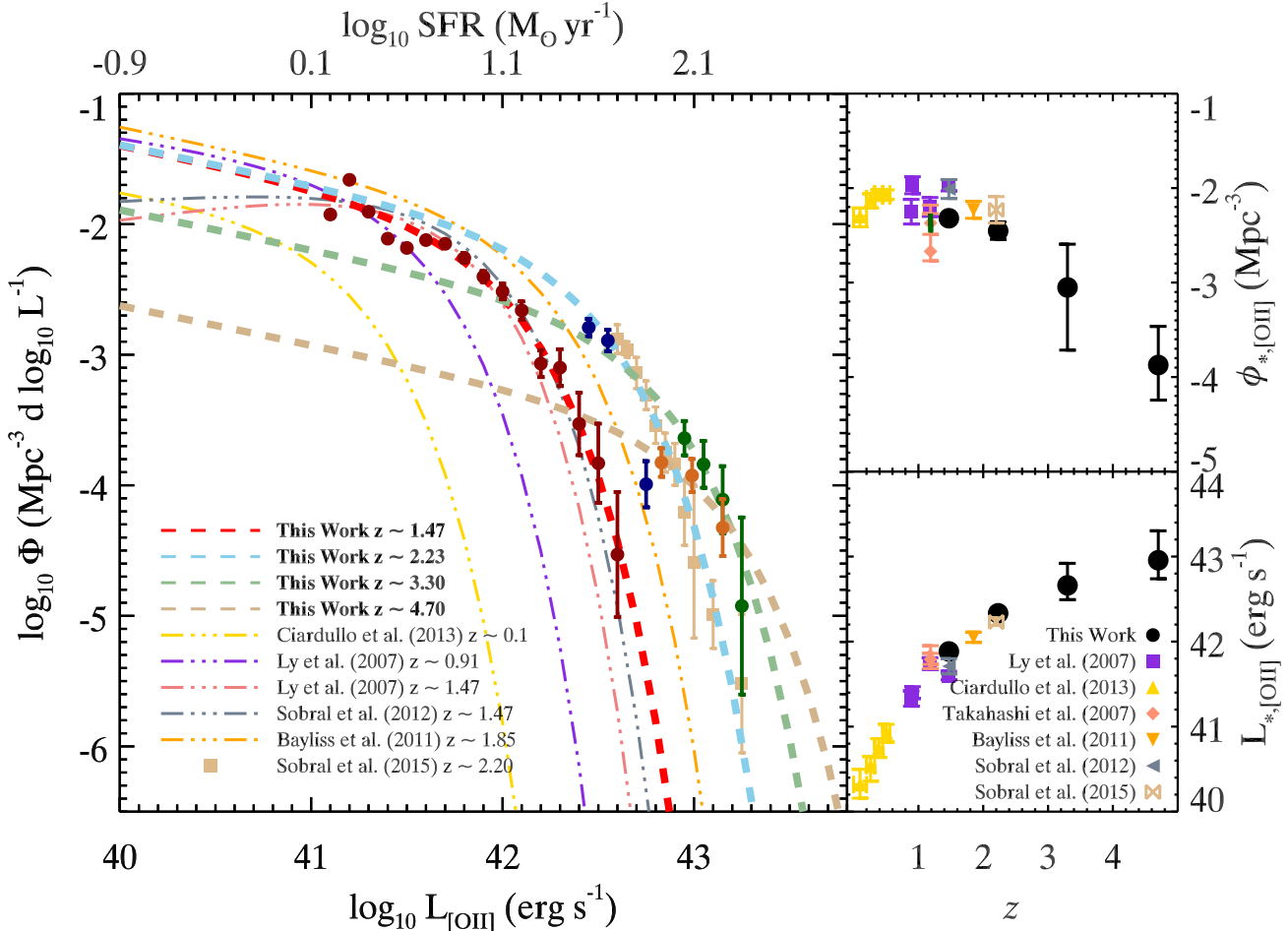


Figure 6. *Left:* Presented are the [OII] Luminosity Functions along with those from the literature. The darker data points are color coded to match the lighter LF fit (*dashed lines*). We find that the evolution from the low- z studies of Gallego et al. (2002) and Ciardullo et al. (2013) to our $z = 4.7$ LFs is quite strong and clear. We find that our $z = 1.47$ LF is in agreement with the HiZELS [OII] study of Sobral et al. (2012) and the Subaru Deep Survey study of Ly et al. (2007). Our $z = 2.23$ is also in agreement with the CF-HiZELS study of Sobral et al. (2015). *Top Right:* The evolution in the normalization of the LF. We find that ϕ_{\star} has been decreasing from $z \sim 1.47$ to $z \sim 5$. *Bottom Right:* The evolution of L_{\star} . We find a clear, strong evolution in L_{\star} all the way to $z \sim 5$.

and Sobral et al. (2012). This is probably due to the fact that both studies used 2'' apertures, while our study uses 3'' apertures to select $z = 1.47$ [OII] emitters, which means that their studies are better at recovering faint emitters.

We find a strong evolution in L_{\star} , as shown in figure 6 for which a strong, rising trend is seen up to $z \sim 5$. We also see the same evolution in H α studies (e.g., Sobral et al. (2012)), where L_{\star} is strongly increasing from $z = 0$ to 5 . The same evolution of L_{\star} is seen in UV studies (Oesch et al. 2010) up to the same redshift range. We notice some scatter for the low- z studies (Ly et al. 2007; Takahashi et al. 2007; Bayliss et al. 2011; Sobral et al. 2012; Ciardullo et al. 2013). This is primarily due to limitations in survey area and/or shallowness of the surveys.

The evolution in ϕ_{\star} is shown in figure 6 along with measurements from the literature. Our measurements show a decreasing trend since $z \sim 1.5$ while for redshifts less than 1.5 shows a flat evolution in ϕ_{\star} . The same evolution in ϕ_{\star} is also seen in H α studies (e.g., Sobral et al. (2013)) where after $z \sim 1$ and up to $z \sim 2$, ϕ_{\star} is shown to be decreasing. UV measurements (Oesch et al. 2010) also see a similar trend.

Future wide surveys, such as EUCLID and WFIRST, will be able to observe larger samples of emission-line galaxies such that our results can be used as predictions for such upcoming projects. Furthermore, our luminosity functions can be used as a tool to gauge the level of low- z interlopers in Ly α studies at high- z . By integrating the luminosity functions, they can determine how many H β +[OIII] and [OII] emitters will be expected in their sample.

4 EVOLUTION OF THE STAR-FORMATION HISTORY OF THE UNIVERSE

In this section, we present the star-formation history evolution of our [OII] sample out to $z \sim 5$. We begin by measuring the level of AGN contamination and then present the calibrations used to get the star-formation rate densities (SFRDs). We conclude with a discussion of the evolution of the SFRD based on [OII] emitters, the correction for dust, and our estimates of the stellar mass density evolution of the universe based on our SFRD fit.

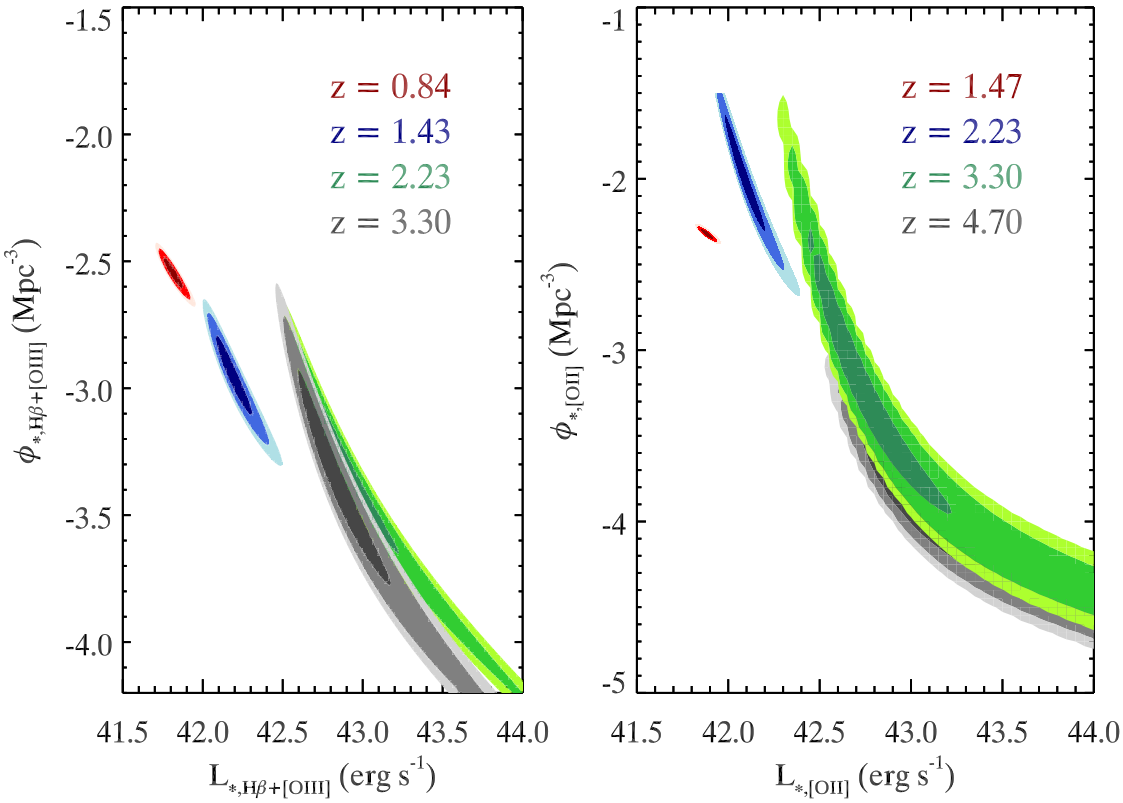


Figure 7. Shown is the interdependent evolution of L_* and ϕ_* for $H\beta+[OIII]$ (left) and $[OII]$ (right). The contours are color-coded to match the text color in the legend. The confidence levels are organized such that the *darkest shade* is the 1σ level and the *lightest shade* being the 3σ level. There is a clear evolution that as redshift increases, ϕ_* drops and L_* increases up to $z \sim 2.23$ and then flattens out at higher redshifts.

Table 3. The Luminosity Function parameters and derived properties for all $H\beta+[OIII]$ and $[OII]$ emitters. Errors in ϕ_* and L_* are computed by running a Monte Carlo Simulation, displacing all the measurements of Φ_{final} by 1σ . The faint-end slope, α , was fixed as our data don't go faint enough to constrain the faint-end properly. The luminosity density, ρ_L , was calculated by taking the infinite integral of the LF. The SFRDs were calculated based on the Kennicutt (1998) calibration ($[OII]$) and Osterbrock & Ferland (2006) ($H\beta+[OIII]$) with $\dot{\rho}_{*,\text{comp}}$ being the completeness and filter profile corrected SFRD measurement. $\dot{\rho}_{*,\text{corr}}$ is the completeness + filter profile + dust corrected SFRD measurement. $\dot{\rho}_{*,\text{AGN-corr}}$ is the completeness + filter profile + dust corrected + AGN corrected SFRD measurement. We show every measurement as $\dot{\rho}_{*,\text{comp}}$ is the most robust measurement, while the dust and dust + AGN corrected measurements are based on assumptions regarding line ratios, dust extinction laws, and AGN selection methods.

| H β +[OIII] Luminosity Function Properties | | | | | | | |
|--|---|---|----------|--|---|---|---|
| z | $\log_{10} \phi_*$ (Mpc^{-3}) | $\log_{10} L_*$ (ergs s^{-1}) | α | $\log_{10} \rho_L$ ($\text{ergs s}^{-1} \text{Mpc}^{-3}$) | $\log_{10} \dot{\rho}_{*,\text{comp}}$ ($\text{M}_\odot \text{yr}^{-1} \text{Mpc}^{-3}$) | $\log_{10} \dot{\rho}_{*,\text{corr}}$ ($\text{M}_\odot \text{yr}^{-1} \text{Mpc}^{-3}$) | $\log_{10} \dot{\rho}_{*,\text{AGN-corr}}$ ($\text{M}_\odot \text{yr}^{-1} \text{Mpc}^{-3}$) |
| 0.84 | $-2.54^{+0.05}_{-0.03}$ | $41.81^{+0.04}_{-0.03}$ | -1.60 | 39.61 | $-1.520^{+0.02}_{-0.01}$ | $-0.980^{+0.02}_{-0.01}$ | $-1.032^{+0.03}_{-0.03}$ |
| 1.42 | $-2.72^{+0.07}_{-0.13}$ | $42.09^{+0.06}_{-0.07}$ | -1.60 | 39.72 | $-1.417^{+0.05}_{-0.04}$ | $-0.877^{+0.05}_{-0.04}$ | $-0.966^{+0.06}_{-0.05}$ |
| 2.23 | $-3.26^{+0.19}_{-0.26}$ | $42.86^{+0.19}_{-0.15}$ | -1.60 | 39.95 | $-1.187^{+0.06}_{-0.06}$ | $-0.647^{+0.06}_{-0.06}$ | $-0.795^{+0.08}_{-0.08}$ |
| 3.24 | $-3.30^{+0.26}_{-0.29}$ | $42.79^{+0.19}_{-0.15}$ | -1.60 | 39.84 | $-1.293^{+0.13}_{-0.07}$ | $-0.753^{+0.13}_{-0.07}$ | $-0.901^{+0.14}_{-0.09}$ |

| [OII] Luminosity Function Properties | | | | | | | |
|--------------------------------------|---|---|----------|--|---|---|---|
| z | $\log_{10} \phi_*$ (Mpc^{-3}) | $\log_{10} L_*$ (ergs s^{-1}) | α | $\log_{10} \rho_L$ ($\text{ergs s}^{-1} \text{Mpc}^{-3}$) | $\log_{10} \dot{\rho}_{*,\text{comp}}$ ($\text{M}_\odot \text{yr}^{-1} \text{Mpc}^{-3}$) | $\log_{10} \dot{\rho}_{*,\text{corr}}$ ($\text{M}_\odot \text{yr}^{-1} \text{Mpc}^{-3}$) | $\log_{10} \dot{\rho}_{*,\text{AGN-corr}}$ ($\text{M}_\odot \text{yr}^{-1} \text{Mpc}^{-3}$) |
| 1.47 | $-2.32^{+0.02}_{-0.01}$ | $41.88^{+0.02}_{-0.02}$ | -1.30 | 39.68 | $-1.176^{+0.01}_{-0.01}$ | $-0.928^{+0.01}_{-0.01}$ | $-1.017^{+0.04}_{-0.04}$ |
| 2.25 | $-2.45^{+0.10}_{-0.09}$ | $42.33^{+0.05}_{-0.03}$ | -1.30 | 39.99 | $-0.862^{+0.07}_{-0.06}$ | $-0.614^{+0.07}_{-0.06}$ | $-0.707^{+0.08}_{-0.07}$ |
| 3.34 | $-3.05^{+0.46}_{-0.66}$ | $42.66^{+0.26}_{-0.17}$ | -1.30 | 39.72 | $-1.131^{+0.38}_{-0.23}$ | $-0.883^{+0.38}_{-0.23}$ | $-0.977^{+0.38}_{-0.24}$ |
| 4.69 | $-3.87^{+0.41}_{-0.37}$ | $42.96^{+0.35}_{-0.22}$ | -1.30 | 39.20 | $-1.657^{+0.12}_{-0.11}$ | $-1.409^{+0.12}_{-0.11}$ | $-1.503^{+0.13}_{-0.12}$ |

4.1 Contribution from AGN

Active Galactic Nuclei (AGN) play an important role in the evolution of galaxies. Because AGN heat the cold gas that is photo-ionized by O & B-type stars in star-forming regions, the same emission-lines become present by both sources. It is then imperative that the SFRDs are properly corrected for AGN contamination to ensure that the sample is, by majority, a star-forming sample. Due to the low number-density of AGNs, it is difficult to use the current catalogs in the literature (e.g., *Chandra-COSMOS*) as a direct indicator on the level of AGN contribution/contamination to our sample. When comparing to *Chandra-COSMOS* (Elvis et al. 2009), we find only 1 AGN and that is in our $z \sim 2.23$ sample. We also compared our catalogs to the *XMM-COSMOS* catalog (Cappelluti et al. 2009) and found no matches.

These matches themselves can not give us a complete indication of the level of our AGN contamination as they are X-ray flux-limited. We instead take advantage of the rest-frame $1.6\mu\text{m}$ bump in the SEDs of star-forming galaxies. This bump arises from the minimum opacity of H^- ions in the stellar atmospheres of cool stars. For AGNs, the bump is meshed in with various other emission (e.g., PAHs, silicate grains) resulting in a rising power-law SED after $1.6\mu\text{m}$ rest-frame. We use the deep IRAC data in COSMOS and UDS and with the condition that redder colors are AGNs, signifying the rising SED after $1.6\mu\text{m}$, and anything with bluer colors are star-forming galaxies resulting in the $1.6\mu\text{m}$ bump. We measure the colors by taking the $[3.6 - 4.5] > 0.1$ ($z \sim 0.8$), $[4.5 - 5.6] > 0.1$ ($z \sim 1.5$), and $[5.6 - 8.0] > 0.1$ ($z \sim 2.2$) for $\text{H}\beta + [\text{OIII}]$ emitters and $[4.5 - 5.6] > 0.1$ ($z \sim 1.47$) and $[5.6 - 8.0] > 0.1$ ($z \sim 2.23$) for $[\text{OII}]$ emitters. We find AGN contamination for $\text{H}\beta + [\text{OIII}]$ is $\sim 11.4\%$, $\sim 18.5\%$, and $\sim 28.8\%$ for $z \sim 0.8$, 1.5 , and 2.2 , respectively. The amount of AGN contamination for $[\text{OII}]$ is $\sim 18.5\%$ and $\sim 19.4\%$ for $z \sim 1.47$ and 2.23 , respectively. For $z > 2.2$ in $[\text{OII}]$ emitters, we set the AGN contamination constant to that at $z = 2.2$ as this would require going beyond the last IRAC band. Note that these are upper limits for the level of AGN contamination such that our SFRDs are corrected for the highest contamination possible via the $1.6\mu\text{m}$ bump technique. By comparing our SFRD measurements to other star-formation tracers, we can determine if the AGN correction was too high or not. But to reliably measure the correction will require follow-up spectroscopy of our sample to properly separate the AGN from the star-forming sample. We therefore apply our determined potential contribution measurements to the luminosity densities measured from the fully integrated LFs and incorporate the AGN correction in the errors by adding 20% of the correction factor in quadrature with the luminosity density errors.

4.2 Calibrations

The star-formation rate density is calculated via the luminosity density from the LF at each redshift. The luminosity density is defined as:

$$\mathcal{L} = \int_0^{\infty} \Phi(L) L dL = \phi_* L_* \Gamma(\alpha + 2) \quad (5)$$

where \mathcal{L} is the luminosity density. Our determined luminosity densities are highlighted in table 3 and consider the

full range of luminosities. The star-formation rate density (SFRD) is then calculated by using the Kennicutt (1998) diagnostics:

$$\dot{\rho}_{\text{SFR}, \text{OII}} = 1.4 \times 10^{-41} \mathcal{L}_{[\text{OII}]} M_{\odot} \text{yr}^{-1} \text{Mpc}^{-3} \quad (6)$$

where a $\mathcal{L}_{[\text{OII}]} / \mathcal{L}_{\text{H}\alpha} = 1.77$ is assumed. We note that using the $[\text{OII}]$ SFR calibration comes with several drawbacks, such as metallicity, reddening, and line ratio assumptions, but the $[\text{OII}]$ line is the brightest emission-line detectable at $z > 1.5$ where $\text{H}\alpha$ falls in the infrared. We will present the effects of these drawbacks in a future study (Khstovan et al. in prep). Furthermore, we present the uncorrected for dust SFRD measurements to see, qualitatively, the evolution of the SFRD. This means that the results shown in figure 8 are lower-limits since any dust correction will just increase the SFRD measurements.

We also use the derived relation of Osterbrock & Ferland (2006):

$$\dot{\rho}_{\text{SFR}, \text{H}\beta + \text{OIII}} = 7.35 \times 10^{-42} \mathcal{L}_{[\text{H}\beta + \text{OIII}]} M_{\odot} \text{yr}^{-1} \text{Mpc}^{-3} \quad (7)$$

to measure the $\text{H}\beta + [\text{OIII}]$ SFRD⁴ although this can not be taken as a purely star-forming indicator as there are several caveats behind it. *We want to make this point specifically clear; we do not use the $\text{H}\beta + [\text{OIII}]$ SFRDs in fitting the star-formation and stellar mass assembly history of the Universe.* We instead use it to compare the measurements to those of the $[\text{OII}]$ SFRDs and other tracers in the literature to show if our sample is tracing a star-forming sample and whether or not if the $\text{H}\beta + [\text{OIII}]$ calibration is more of a “reliable” tracer of star-formation activity than previously thought.

4.3 Star-Formation Rate Density Evolution of $[\text{OII}]$ Emitters

4.3.1 Uncorrected-for-Dust

Figure 8 shows the evolution of the uncorrected-for-dust $[\text{OII}]$ SFR density for the first time and determined in a self-consistent way from $z = 0 - 5$. The evolution is clear and signifies that a peak that occurs at $z \sim 2 - 3$ and then there is a fall for higher redshifts. We include $[\text{OII}]$ measurements from the literature after uncorrecting them for dust and correcting the cosmology (the pre-2000 papers used non- ΛCDM cosmological parameters). These results plus ours can then be taken as a lower limit as any dust extinction correction would increase the SFR densities. We include a compilation of SFR densities and LF parameters from various studies, using various diagnostics, all normalized to the same cosmology as that of this paper, same Kennicutt (1998) calibration with the same line ratio, and all with $A_{[\text{OII}]} = 0$ to make it easier for future studies to utilize. This compilation is found in appendix C. We find that our $z = 1.47$ $[\text{OII}]$ SFRD measurement is in perfect agreement with Sobral et al. (2012) and Ly et al. (2007). We are also in perfect agreement with the measurement of Sobral et al. (2015) and our $z = 2.23$ measurement.

⁴ We used the dust extinction curve of Calzetti et al. (2000) for the $\text{H}\beta + [\text{OIII}]$ emitters and applied for all redshifts, such that $A_{\text{H}\beta + [\text{OIII}]} = 1.35$ mag (assuming $A_{\text{H}\alpha} = 1.0$ mag).

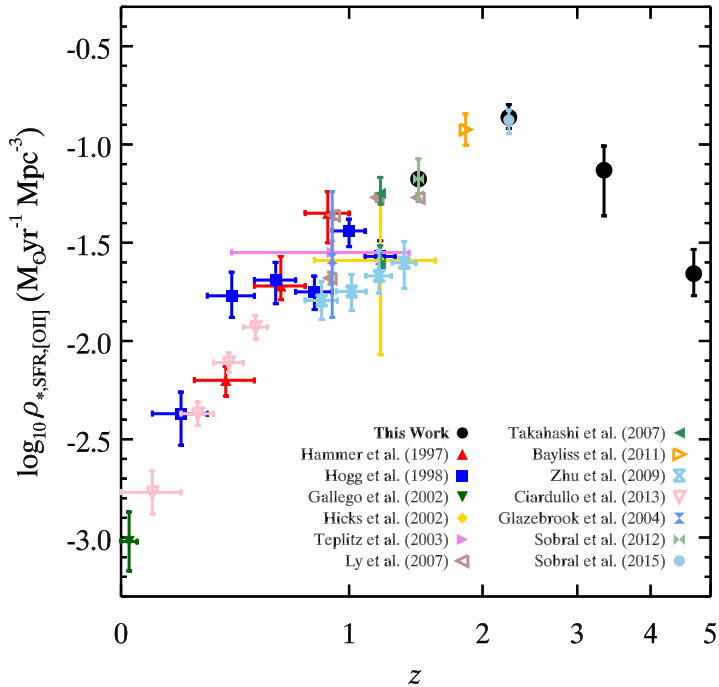


Figure 8. The uncorrected for dust SFRD evolution based only on [OII] emission studies. We find that our $z = 1.47$ and 2.23 LF continues the inverse power-law slope that is found from $z = 0 - 2$ in the majority of SFRD studies, and a continuous drop for $z > 2$. This is the first time that [OII] studies have gone beyond $z \sim 1.5$ in a reasonably, statistically constrained fashion. We find perfect agreement with Sobral et al. (2013) and are 0.1 dex off from Ly et al. (2007). Also, we find perfect agreement with the $z = 2.25$ SFRD of Sobral et al. (2015).

We note that Bayliss et al. (2012) made a measurement at $z = 4.6$ by observing the GOODS-S field using the NB2090 and Ks filters of the ESO HAWK-I instrument. The results of this study are restricted to a sample of only 3 genuine emitters. Although ground-breaking at the time, their SFRD estimate is severely limited by issues of sample size and cosmic variance.

4.3.2 Dust & AGN Corrected SFRD

To compare with other studies using different SFRD diagnostics, we adopt the dust correction using the HiZELS $z = 1.47$ measurement of Hayashi et al. (2013), $A_{H\alpha} \sim 0.35$ mag. Hayashi et al. (2013) studied $H\alpha$ and [OII] emitters using HiZELS data to conclude that the traditional $A_{H\alpha} = 1.0$ mag that has been used in the literature is overestimating the dust correction for [OII] emitters at $z = 1.47$, such that these emitters are observed to have $A_{H\alpha} \sim 0.35$ mag and are less dusty than previously thought.

To test the dust extinction coefficient of Hayashi et al. (2013), we apply the $A_{H\alpha} \sim 1.0$ mag to all four [OII] SFRD measurements. We find that the measurements overestimated the $H\alpha$ -based SFRD measurements of Sobral et al. (2013) and the radio-stacked measurements of Karim et al. (2011), which is impervious to dust extinction. The level

of overestimation is such that our $z = 1.47$ SFRD measurement and $z = 2.23$ SFRD measurement was ~ 0.4 dex above the SFRD measurements of Sobral et al. (2013) and Karim et al. (2011). When using the Hayashi et al. (2013) dust extinction coefficient, we find that our SFRD measurements are perfectly matched with Sobral et al. (2013) and Karim et al. (2011), as seen in figure 9.

We apply the Calzetti correction (Calzetti et al. 2000) such that:

$$\frac{A_{[OII]}}{A_{H\alpha}} = \frac{k([OII])}{k(H\alpha)} \quad (8)$$

where $k([OII]) = 5.86$ and $k(H\alpha) = 3.31$, resulting in $A_{[OII]} = 0.62$ mag. We calibrate all the measurements to the same [OII] SFR calibration of Kennicutt (1998). All measurements hereinafter include AGN corrections as discussed in section 4.1.

Figure 9 shows our dust-corrected and AGN-corrected [OII] SFRD measurements. We also include a large compilation of studies from the literature which is a combination of the compilations of Hopkins & Beacom (2006), Madau & Dickinson (2014), Gunawardhana et al. (2013), Ly et al. (2007), and our own compilation as a comparison (appendix C). We find that our measurements accurately reproduce the star-formation history of the universe up to $z \sim 5$. This is the first time that an [OII] study has ever accomplished such a measurement in a self-consistent manner. We find that the $z = 1.47$ and 2.23 perfectly agree with the HiZELS $H\alpha$ measurements of Sobral et al. (2013) on figure 9. The AGN contamination in Sobral et al. (2013) assumed a simple $\sim 10\%$, which is backed by a detailed search of potential AGNs by Garn et al. (2010). Based on the similarities between our [OII] measurement and the independently AGN-corrected SFRD measurement of Sobral et al. (2013), we can conclude that the level of AGN contamination measured is reasonable and the methodology sound.

Another key point is the stacked radio measurements of Karim et al. (2011) (pink squares on figure 9). The benefit of radio measurements are that they are impervious to dust, but have the downside of poor resolution and blending. We find that our $z = 1.47$ and $z = 2.23$ [OII] measurements are in agreement with Karim et al. (2011), such that the Hayashi et al. (2013) dust extinction coefficient does reliably correct our measurements to represent the dust-corrected SFRD of star-forming galaxies.

We also find an interesting result when comparing the $H\beta+[OIII]$ SFRD measurements to our [OII] SFRDs and other measurements in the literature. As discussed above, the $H\beta+[OIII]$ calibration is considered in the literature as a “mixed” tracer of star-formation activity. Here we find that using the calibration of Osterbrock & Ferland (2006) with a $A_{H\beta+[OIII]} = 1.35$ mag, our $H\beta+[OIII]$ measurement for $z = 0.84$ matches perfectly with the $H\alpha$ SFRD of Sobral et al. (2013) and the radio measurement of Karim et al. (2011). This also implies that the AGN correction applied to this measurement was accurate the independently AGN-corrected $H\alpha$ measurement. For our $z = 1.43$ $H\beta+[OIII]$ SFRD, we find a perfect match with Karim et al. (2011), Sobral et al. (2012), Sobral et al. (2013), and our [OII] SFRD. The $z = 2.23$ $H\beta+[OIII]$ SFRD matches well with Karim et al. (2011), Sobral et al. (2012), and our [OII] SFRD measurement. Lastly, we find perfect agree-

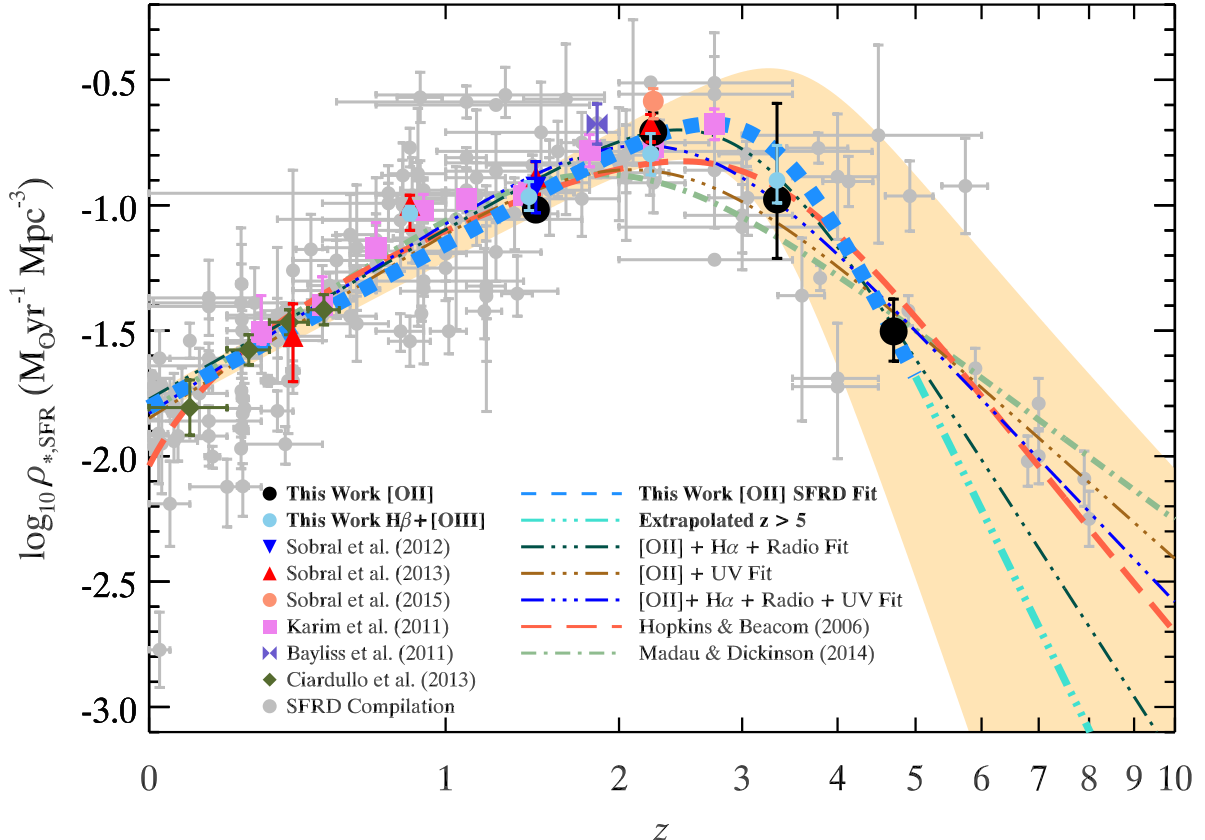


Figure 9. Our [OII] dust & AGN corrected SFRD evolution with the [OII] studies of Bayliss et al. (2011); Ciardullo et al. (2013); Sobral et al. (2013) and Sobral et al. (2015), along with the results of this paper, that are used to fit the parametrization of Madau & Dickinson (2014). The best fit is shown as the dashed line (*dodger blue*) and is only based on [OII] measurements. We also include an extrapolation to higher- z (*dashed-dotted turquoise* line), as we don't constrain this part of redshift space but can extrapolate based on our fit. The $1-\sigma$ region is highlighted in *gold* filled regions around the fit. The stacked radio study of Karim et al. (2011) and the $H\alpha$ study of Sobral et al. (2013) are also shown as a comparison and are in agreement with our measurements. Our compilation of SFRD measurements (in *gray*) are a combination of our compilation and that of Hopkins & Beacom (2006), Madau & Dickinson (2014), Ly et al. (2007), and Gunawardhana et al. (2013). We reproduce the SFRD evolution history of the universe based primarily on [OII] studies with the peak of star-formation history occurring at $z \sim 3$. We also include the fits of Hopkins & Beacom (2006) (IMF corrected to Salpeter) and that of Madau & Dickinson (2014). We find that the Hopkins & Beacom (2006) fit reasonably matches our SFRD fit, while the Madau & Dickinson (2014) fits well until $z > 2$. This is mostly because the Madau & Dickinson (2014) fit is driven by the $z > 5$ UV measurements (which are not backed by spectroscopy), for which we do not include in our [OII] fit.

ment between our [OII] SFRD and the $H\beta+[OIII]$ SFRD at $z \sim 3.3$. All these perfect agreements hints to the notion that the $H\beta+[OIII]$ SFR calibrations could in fact be more of a reliable tracer of star-formation activity than previously thought. Furthermore, this is also strong evidence to show that our $H\beta+[OIII]$ sample is dominated by star-forming galaxies and is a reliable sample.

We fit the SFRD using our [OII] SFRD measurements along with the [OII] measurements of Bayliss et al. (2011); Ciardullo et al. (2013) and Sobral et al. (2012) to the parametrization of Madau & Dickinson (2014):

$$\log_{10} \rho_* = a \frac{(1+z)^b}{1 + [(1+z)/c]^d} \text{ M}_\odot \text{ yr}^{-1} \text{ Mpc}^{-3} \quad (9)$$

where our fit results with $a = 0.016 \pm 0.002$, $b = 2.16 \pm 0.17$, $c = 4.23 \pm 0.53$, and $d = 10.22 \pm 3.96$. The fit is purely

based on [OII] emitters, but we have also fitted for the cases of [OII]+ $H\alpha$ +Radio, [OII]+UV, and [OII]+ $H\alpha$ +Radio+UV (see figure 9) to show how our fit will vary based on the data that we use. Based on the [OII] fit, we see a drop at $z > 3$ that is slightly steeper than those determined by UV dropout studies (i.e., Bouwens et al. 2011, 2014; Oesch et al. 2010; Schenker et al. 2013). Despite the steeper drop in our [OII] SFRD compared to the UV studies, we do find that the UV measurements are still within 1σ .

An important note to make though is that prior to this paper, there does not exist a study besides UV/ $Ly\alpha$ studies that have measured the SFRD up to $z \sim 5$. Our current measurements are the farthest that we can measure the [OII] SFRD due to the fact that the emission line would go past K-band and into the infrared. Future space-based

narrow-band surveys, such as *JWST* and the Wide-field Imaging Surveyor for High-redshift (*WISH*), will be able to probe $[OII]$ emitters up to $z \sim 12$, which would allow us to compare and confirm the UV SFRD measurements at $z > 5$.

We also compare our fit to those of Hopkins & Beacom (2006) and Madau & Dickinson (2014) in figure 9. For the $z < 2$ regime, we find that our $[OII]$ SFRD fit agrees well with all the other fits. For the $z > 2$ regime, we do see divergences based on the fit. In terms of the actual data points, we find that the Hopkins & Beacom (2006) is closest in agreement as it has a continuing SFRD up to a peak at $z \sim 2.5$ and a drop that continues through the high- z $[OII]$ measurements. The Madau & Dickinson (2014) is also in agreement for the high- z measurements, but fails to match with the $z \sim 2 - 3$ peak. This is mostly due to the fact that their measurements are driven by the $z > 5$ UV dropout SFRDs (e.g., Bouwens et al. 2011, 2014; Oesch et al. 2010; Schenker et al. 2013).

As with all SFR measurements, there are systematic uncertainties that must be taken into account. In the case of $[OII]$ emitters, our main systematic uncertainties come from metallicity and dust extinction. To study the metallicities and its effects on the star-formation rate calibration, we will need to conduct follow-up spectroscopy. Furthermore, studying the metallicity of our sample will give us also an understanding of the dynamics (inflow/outflow) that can affect star-formation activity. We also plan to study in a future paper the dust extinction properties of our sample and how it relates to and affects the star-formation activity of galaxies in our sample (Khostovan et al., in prep).

4.4 Evolution of the Stellar Mass Density

We use the $[OII]$ SFRD results presented in this paper to provide an estimate of the stellar mass density (SMD) evolution by doing a time-integral of equation 9. The SMD evolution gives us an understanding of how the universe has assembled its mass throughout cosmic time. This estimate is quantitatively sensitive to the choice of the IMF in terms of the normalization of the SFRD and SMD evolution, but it does not qualitatively affect the final results.

Our estimate assumes a Salpeter IMF, which has been used throughout this entire paper, and a recycling fraction of $R = 0.27$. For a review of the derivation of this factor, we refer the reader to the recent review of Madau & Dickinson (2014). We calculate the SMD by:

$$\rho_*(z) = (1 - R) \int_z^\infty \frac{\dot{\rho}_*(z)}{H_0(1+z)\sqrt{\Omega_M(1+z)^3 + \Omega_\Lambda}} dz \quad (10)$$

where $\dot{\rho}_*(z)$ is the SFRD fit using the parametrization defined in equation 9 and R is the recycling fraction, or the fraction of stars that is returned back into the ISM and IGM. Because the equation above is using $z = \infty$ as a reference for which we do not know the SMD for, we instead constrain the integral such that at $z = 0$ the SMD will be $\log_{10} \rho_* \sim 8.6 \text{ M}_\odot \text{ Mpc}^{-3}$, in agreement with measurements made at that redshift.

Our results are shown in figure 10. We find an evolution where the stellar mass assembly rapidly increases from 6.2 to $8 \text{ M}_\odot \text{ Mpc}^{-3}$ from $z \sim 5$ to 2 , a time frame of only 2 Gyr. The evolution then tapers and flattens out by $z = 0$ which is related to the decrease in the

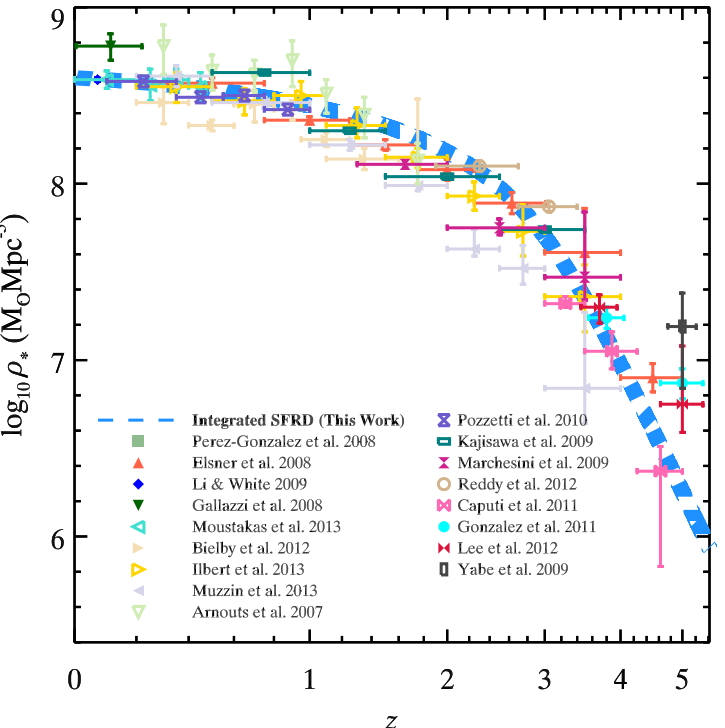


Figure 10. The evolution of the stellar mass density of the Universe based on the integrated $[OII]$ SFRD. Overlaid are the SMD measurements from the literature that were compiled in the recent review of Madau & Dickinson (2014). We find that our integration of the purely $[OII]$ determined SFRD reasonably traces the stellar mass assembly of the Universe.

SFRD that we have observed since $z \sim 2$. This is also the same conclusion found by observational studies of the SMD. We include measurements from Arnouts et al. (2007), Elsner, Feulner & Hopp (2008), Gallazzi et al. (2008), Pérez-González et al. (2008), Kajisawa et al. (2009), Li & White (2009), Marchesini et al. (2009), Yabe et al. (2009), Pozzetti et al. (2010), Caputi et al. (2011), González et al. (2011), Bielby et al. (2012), Lee et al. (2012), Reddy et al. (2012), Ilbert et al. (2013), Moustakas et al. (2013), and Muzzin et al. (2013) in figure 10 and we find that our integrated SFRD reproduces the same evolution seen by these studies. We have found that the $[OII]$ based SFRD and SMD accurately reproduce the evolution of mass assembly in the Universe. This match can also be seen as yet another verification that our sample of $[OII]$ emitters are primarily star-forming galaxies as the conclusions from our SMD estimate are the same seen in the literature.

5 CONCLUSIONS

We have presented the largest sample of $H\beta+[OIII]$ and $[OII]$ emitters between $z \sim 0.8 - 5$ that have been selected based on a robust and self-consistent technique, backed up by a wide array of spectroscopic emitters. We have used the HiZELS UKIRT and Subaru narrow-band catalogs, along with multi-wavelength data from the COSMOS and UDS

fields, to create a clean and well-defined sample of star-forming galaxies. The main results of this paper are as follows:

(i) We have robustly selected a total of 2149, 307, 329, 176 $H\beta+[OIII]$ emitters at $z = 0.84, 1.47, 2.23$, and 3.3 and 3650, 125, 28, 10 $[OII]$ emitters at $z = 1.47, 2.23, 3.3$, and 4.7 in the combined COSMOS and UDS fields. These are the largest samples of $H\beta+[OIII]$ and $[OII]$ emitters to have been detected in this redshift range.

(ii) We have extended the luminosity function in the literature to higher- z , as well as refined the lower- z measurements for both types of emitters. For the $H\beta+[OIII]$ emitters, we find that the bright-end of our $z = 1.47$ and $z = 2.23$ LFs are in agreement with the grism spectroscopy-based luminosity functions of Colbert et al. (2013); hence, this increases the reliability of our sample being dominantly $[OIII]$ emitters in the bright-end. We also find from our predictions of the $[OIII]$ LFs that our sample is dominated by $[OIII]$ emitters at the bright-end. The faint-end is dominated by $H\beta$ emitters. We also find that the normalization of the $[OIII]$ LF is decreasing as redshift increases, signifying that we might be seeing one or a combination of these scenarios: (a) the population of $H\beta$ emitters increases with redshift, (b) the population of $[OIII]$ emitters is increasing, and/or (c) there is some evolution in metallicity that causes the drop.

(iii) The evolution of L_* and ϕ_* for $H\beta+[OIII]$ is found to have a strong increasing/decreasing evolution, respectively, up to $z \sim 2$ and then flattens out at $z \sim 3$. For our $[OII]$ sample, we find that L_* increases strongly up to $z \sim 5$ and ϕ_* is strongly dropping up to the same redshift.

(iv) We have discussed that our luminosity functions are reliable to be used in making predictions of the number of emitters to be detected by future wide-surveys, such as EUCLID and WFIRST. Furthermore, our luminosity functions can also determine the number of low- z interlopers in $Ly\alpha$ studies, such that the level of contamination by low- z sources can be reduced in such studies.

(v) The SFRD has been constrained using $[OII]$ measurements up to $z \sim 5$ for the first time. We find that the peak of the cosmic SFRD is located around $z \sim 3$ and is in agreement with our large compilation of UV, IR, radio, and nebular emission studies. We find that for $z > 2$, our SFRD fit drops slightly faster in comparison to the UV dropout studies in this redshift regime. However, we find that the UV measurements are within the $1-\sigma$ error bar range of our SFRD fit. Future space-based narrow-band surveys, such as *JWST* and *WISH*, will be able to extend the range of $[OII]$ detection out to $z \sim 12$ so that we can compare and confirm or invalidate the UV dropout measurements.

(vi) We also find that the $H\beta+[OIII]$ SFRD measurements are nicely in line with our $[OII]$ sample and other star-formation tracers. This then brings to question of whether the $H\beta+[OIII]$ calibration is more “reliable” as a tracer of star-formation than previously thought. With our large sample of these emitters, we will have the ability to explore this issue in detail.

(vi) By integrating the SFRD, we have made estimates of the stellar mass density evolution and find that it steeply rose up to $z \sim 2$ and flattened out up to the present-day. This is also confirmed by the wealth of measurements in the literature.

The results in the paper have implications in the evolution of galaxies and the star-formation activity occurring in said galaxies. Despite the robustness of our sample, there is still room for improvement. Our measurements have done well to constrain the bright-end, while keeping the faint-end fixed based on measurements from the literature. We will require deeper narrow-band and broad-band measurements in order to constrain the faint-end slope of the LF. Spectroscopic follow-up will also be necessary to accurately measure the extent of AGN contamination in our sample. Although, our color-color selections have shown (see figure A1) that they are quite reliable due to the large set of spectroscopic measurements confirming this reliability. That being said, spectroscopic measurements of our sample will help in separating the $H\beta$ and $[OIII]$ samples to measure separate luminosity functions. Lastly, future narrow-band surveys, such as the proposed *WISH* telescope, will be able to extend the redshift window of $H\beta+[OIII]$ and $[OII]$ studies up to $z \sim 12$, which can be used to confirm the UV dropout studies at higher- z . Despite all these improvements and potential future progresses, our sample has reliably (given all the limitations) and robustly traced the evolution of star-forming activity in the universe.

ACKNOWLEDGMENTS

We acknowledge Anahita Alavi for many useful and insightful discussion regarding the determination of the luminosity function. We also acknowledge Brian Siana for useful comments.

The data used in this paper is publicly available from Sobral et al. (2013). We refer the reader to this paper for details in regards to the data reduction and selection methodology for the original catalogs.

This paper uses data from the VIMOS Public Extragalactic Redshift Survey (VIPERS). VIPERS has been performed using the ESO Very Large Telescope, under the “Large Programme” 182.A-0886. The participating institutions and funding agencies are listed at <http://vipers.inaf.it>

DS acknowledges financial support from the Netherlands Organisation for Scientific research (NWO) through a Veni fellowship, from FCT through a FCT investigator Starting Grant and Start-up Grant (IF/01154/2012/CP0189/CT0010) and from FCT grant PEst-OE/FIS/UI2751/2014

IRS acknowledges support from STFC (ST/L00075X), the ERC Advanced Investigator programme DUSTY GAL 321334, and a Royal Society/Wolfson Merit Award.

PNB acknowledges support from STFC.

REFERENCES

- Arnouts S. et al., 2007, A&A, 476, 137
- Bayliss K. D., McMahon R. G., Venemans B. P., Banerji M., Lewis J. R., 2012, MNRAS, 426, 2178
- Bayliss K. D., McMahon R. G., Venemans B. P., Ryan-Weber E. V., Lewis J. R., 2011, MNRAS, 413, 2883
- Bielby R. et al., 2012, A&A, 545, A23
- Bongiorno A. et al., 2010, A&A, 510, A56
- Bouwens R. J. et al., 2014, ApJ, 795, 126

Bouwens R. J. et al., 2011, ApJ, 737, 90
Bradshaw E. J. et al., 2013, MNRAS, 433, 194
Brammer G. B., van Dokkum P. G., Coppi P., 2008, ApJ, 686, 1503
Bunker A. J., Warren S. J., Hewett P. C., Clements D. L., 1995, MNRAS, 273, 513
Calzetti D., 2013, Star Formation Rate Indicators, Falcón-Barroso J., Knapen J. H., eds., p. 419
Calzetti D., Armus L., Bohlin R. C., Kinney A. L., Koornneef J., Storchi-Bergmann T., 2000, ApJ, 533, 682
Cappelluti N. et al., 2009, A&A, 497, 635
Caputi K. I., Cirasuolo M., Dunlop J. S., McLure R. J., Farrah D., Almaini O., 2011, MNRAS, 413, 162
Ciardullo R. et al., 2013, ApJ, 769, 83
Cirasuolo M. et al., 2007, MNRAS, 380, 585
Coil A. L. et al., 2011, ApJ, 741, 8
Colbert J. W. et al., 2013, ApJ, 779, 34
Cole S. et al., 2001, MNRAS, 326, 255
Darvish B., Sobral D., Mobasher B., Scoville N., Best P., Sales L., Smail I., 2014, ArXiv e-prints
Dickinson M., 1998, in The Hubble Deep Field, Livio M., Fall S. M., Madau P., eds., p. 219
Elsner F., Feulner G., Hopp U., 2008, A&A, 477, 503
Elvis M. et al., 2009, ApJS, 184, 158
Fujita S. S. et al., 2003, ApJL, 586, L115
Gallazzi A., Brinchmann J., Charlot S., White S. D. M., 2008, MNRAS, 383, 1439
Gallego J., García-Dabó C. E., Zamorano J., Aragón-Salamanca A., Rego M., 2002, ApJL, 570, L1
Garilli B. et al., 2014, A&A, 562, A23
Garn T. et al., 2010, MNRAS, 402, 2017
Geach J. E., Smail I., Best P. N., Kurk J., Casali M., Ivison R. J., Coppin K., 2008, MNRAS, 388, 1473
Geach J. E., Sobral D., Hickox R. C., Wake D. A., Smail I., Best P. N., Baugh C. M., Stott J. P., 2012, MNRAS, 426, 679
Glazebrook K., Tober J., Thomson S., Bland-Hawthorn J., Abraham R., 2004, AJ, 128, 2652
González V., Labbé I., Bouwens R. J., Illingworth G., Franx M., Kriek M., 2011, ApJL, 735, L34
Gunawardhana M. L. P. et al., 2013, MNRAS, 433, 2764
Hammer F. et al., 1997, ApJ, 481, 49
Hayashi M., Sobral D., Best P. N., Smail I., Kodama T., 2013, MNRAS, 430, 1042
Hicks E. K. S., Malkan M. A., Teplitz H. I., McCarthy P. J., Yan L., 2002, ApJ, 581, 205
Hogg D. W., Cohen J. G., Blandford R., Pahre M. A., 1998, ApJ, 504, 622
Hopkins A. M., Beacom J. F., 2006, ApJ, 651, 142
Ilbert O. et al., 2009, ApJ, 690, 1236
Ilbert O. et al., 2013, A&A, 556, A55
Johnston R., 2011, A&AR, 19, 41
Kajisawa M. et al., 2009, ApJ, 702, 1393
Karim A. et al., 2011, ApJ, 730, 61
Kennicutt R. C., Evans N. J., 2012, ARA&A, 50, 531
Kennicutt, Jr. R. C., 1998, ARA&A, 36, 189
Lawrence A. et al., 2007, MNRAS, 379, 1599
Lee K.-S. et al., 2012, ApJ, 752, 66
Li C., White S. D. M., 2009, MNRAS, 398, 2177
Lilly S. J., Le Fevre O., Hammer F., Crampton D., 1996, ApJL, 460, L1
Lilly S. J. et al., 2007, ApJS, 172, 70
Ly C., Lee J. C., Dale D. A., Momcheva I., Salim S., Staudaher S., Moore C. A., Finn R., 2011, ApJ, 726, 109
Ly C. et al., 2007, ApJ, 657, 738
Madau P., Dickinson M., 2014, ARA&A, 52, 415
Marchesini D., van Dokkum P. G., Förster Schreiber N. M., Franx M., Labbé I., Wuyts S., 2009, ApJ, 701, 1765
Markwardt C. B., 2009, in Astronomical Society of the Pacific Conference Series, Vol. 411, Astronomical Data Analysis Software and Systems XVIII, Bohlender D. A., Durand D., Dowler P., eds., p. 251
McLure R. J. et al., 2013, MNRAS, 428, 1088
Moustakas J. et al., 2013, ApJ, 767, 50
Muzzin A. et al., 2013, ApJ, 777, 18
Oesch P. A. et al., 2010, ApJL, 725, L150
Osterbrock D. E., Ferland G. J., 2006, Astrophysics of gaseous nebulae and active galactic nuclei
Pascual S., 2005, PASP, 117, 120
Pérez-González P. G. et al., 2008, ApJ, 675, 234
Pirzkal N. et al., 2013, ApJ, 772, 48
Pozzetti L. et al., 2010, A&A, 523, A13
Reddy N. A., Pettini M., Steidel C. C., Shapley A. E., Erb D. K., Law D. R., 2012, ApJ, 754, 25
Schenker M. A. et al., 2013, ApJ, 768, 196
Scoville N. et al., 2007, ApJS, 172, 1
Smit R., Bouwens R. J., Franx M., Illingworth G. D., Labbé I., Oesch P. A., van Dokkum P. G., 2012, ApJ, 756, 14
Sobral D., Best P. N., Geach J. E., Smail I., Cirasuolo M., Garn T., Dalton G. B., Kurk J., 2010, MNRAS, 404, 1551
Sobral D. et al., 2009, MNRAS, 398, 75
Sobral D., Best P. N., Matsuda Y., Smail I., Geach J. E., Cirasuolo M., 2012, MNRAS, 420, 1926
Sobral D., Best P. N., Smail I., Geach J. E., Cirasuolo M., Garn T., Dalton G. B., 2011, MNRAS, 411, 675
Sobral D., Best P. N., Smail I., Mobasher B., Stott J., Nisbet D., 2014, MNRAS, 437, 3516
Sobral D. et al., 2015, MNRAS, submitted
Sobral D., Smail I., Best P. N., Geach J. E., Matsuda Y., Stott J. P., Cirasuolo M., Kurk J., 2013, MNRAS, 428, 1128
Stark D. P., Ellis R. S., Bunker A., Bundy K., Targett T., Benson A., Lacy M., 2009, ApJ, 697, 1493
Stott J. P. et al., 2013a, MNRAS, 436, 1130
Stott J. P., Sobral D., Smail I., Bower R., Best P. N., Geach J. E., 2013b, MNRAS, 430, 1158
Swinbank A. M., Smail I., Sobral D., Theuns T., Best P. N., Geach J. E., 2012a, ApJ, 760, 130
Swinbank A. M., Sobral D., Smail I., Geach J. E., Best P. N., McCarthy I. G., Crain R. A., Theuns T., 2012b, MNRAS, 426, 935
Takahashi M. I. et al., 2007, ApJS, 172, 456
Teplitz H. I., Collins N. R., Gardner J. P., Hill R. S., Rhodes J., 2003, ApJ, 589, 704
Tresse L., Maddox S. J., Le Fèvre O., Cuby J.-G., 2002, MNRAS, 337, 369
Villar V., Gallego J., Pérez-González P. G., Pascual S., Noeske K., Koo D. C., Barro G., Zamorano J., 2008, ApJ, 677, 169
Yabe K., Ohta K., Iwata I., Sawicki M., Tamura N., Akiyama M., Aoki K., 2009, ApJ, 693, 507
Zhu G., Moustakas J., Blanton M. R., 2009, ApJ, 701, 86

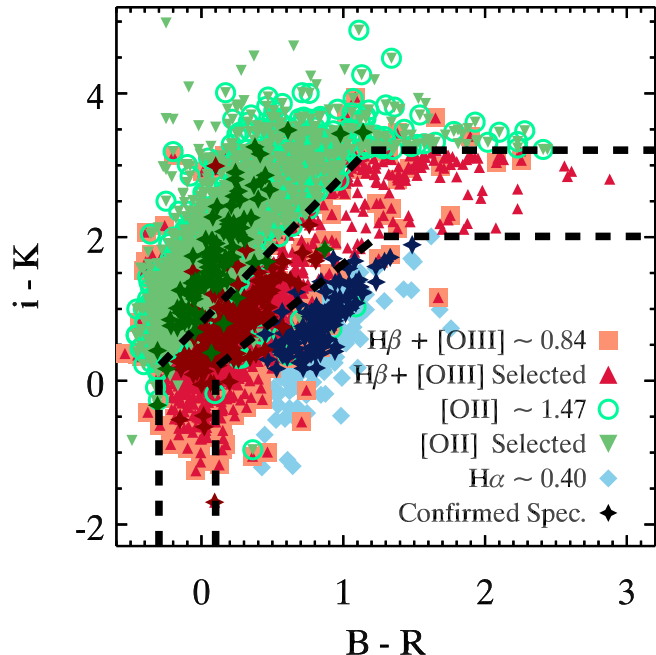


Figure A1. The $i - K$ versus $B - R$ color-color distribution of NB921 emitters using the color-color selection of Sobral et al. (2013). Overall, the level of completeness is $> 90\%$ as the large majority of spectroscopically confirmed emitters are within the selection area; hence, we confirm the the $BRiK$ selection of Sobral et al. (2009) is very efficient in selecting $H\alpha$, $H\beta+[OIII]$, and $[OII]$ samples from narrow-band surveys.

APPENDIX A: SELECTION TECHNIQUE

Here, we present, in detail, the selection of emitters that made it in to our sample. We also present the exact color-color selections that were applied in our work in table A1.

A0.1 $H\beta+[OIII]$ Emitters at $z \sim 0.8$

$H\beta+[OIII]$ sources in the NB921 data at $z \sim 0.8$ are selected by their photometric redshifts within the range of $0.75 < z_{phot} < 0.95$. The color-color selection criterion reduces the number of contaminants by separating the $H\beta+[OIII]$ emitters from lower- z $H\alpha$ and higher- z $[OII]$ emitters. This is done by using the $BRiK$ selection (Sobral et al. 2009) in figure A1. Spectroscopic redshifts were used to assess the robustness and effectiveness of the selection criteria. 213 sources were spectroscopically confirmed. 169 were selected by the color-color selection. From the 213 sources (for which all were selected by their photo- z), only 11 were confirmed $H\beta$ 4861, 76 were $[OIII]$ 4959, and 126 were $[OIII]$ 5007 emitters. Removed from the sample where 7 low- z and 14 high- z spectroscopically confirmed emitters. The lower- z emitters were primarily $H\alpha$ and $[NII]$. The higher- z emitters were primarily $[OII]$ emitters. All these misidentified emitters were removed from the sample. Based on the spectroscopic data, we find that $\sim 91\%$ of all spectroscopic measurements for photo- z selected objects were either $H\beta$ or $[OIII]$ emitters and that the $BRiK$ color-color selection does select $\sim 91\%$ of all the $H\beta+[OIII]$ spectroscopically confirmed emitters. In total, we have 2676 $z = 0.84$ $H\beta+[OIII]$ emitters in our sample. Based on the spectroscopic data, we find that the color-

color selection effectively selects $H\beta+[OIII]$ emitters with a completeness of $\sim 91\%$, making our sample not just the largest, but the most complete sample of $H\beta+[OIII]$ emitters to date.

A0.2 $H\beta+[OIII]$ & $[OII]$ Emitters at $z \sim 1.5$

$[OII]$ emitters in NB921 are selected with photometric redshifts between $1.25 < z_{phot} < 1.65$. We use the $BRiK$ color-color selection and include any sources with spectroscopic redshifts. Included in our sample are 97 spectroscopically confirmed sources, with 90 of them being color-color selected as well. Removed from the sample were 48 low- z spectroscopically confirmed emitters, for which the majority were $[OIII]$. We also removed a few $[HeI]$ emitters at $z \sim 1.28$ and $H\alpha$, and $[NII]$ emitters ($z \sim 0.4$). The contamination from high- z emitters was significantly less (8 emitters) as there are no major emission lines beyond $[OII]$. The majority of this contamination came from $[MgII]$ emitters at $z = 2.25$. The issue of contamination arises here as we may “naively” state that our level of contamination is $\sim 33\%$, but it is noted that spectroscopic measurements to date have an inherent bias to the low- z regime, such that there are more low- z than high- z measurements. This makes accurately measuring the level of contamination difficult. We note though that our color-color selection did select $\sim 93\%$ of the spectroscopically confirmed emitters. In total, we have selected 3149 $z = 1.47$ $[OII]$ emitters. This is by far the largest sample of $[OII]$ emitters at $z \sim 1.5$ to date and, based on the spectroscopically confirmed sources, is $\sim 93\%$ complete.

$H\beta+[OIII]$ emitters in NBJ are selected based on a photometric redshift range of $1.20 < z_{phot} < 1.70$. The color-color selection criteria consists of a BzK and izK selection, as shown in figure A2. We use the BzK selection to get our initial sample of emitters and remove the lower- z contaminants, which are mostly $H\alpha$ emitters. To remove the higher- z contaminants ($[OII]$), we use the izK selection. There were also 15 spectroscopically confirmed sources, all of which were within our color-color selection. Of these 15 emitters, 4 were $H\beta$, 5 $[OIII]$ 4958, and 6 $[OIII]$ 5007 emitters. We removed 5 emitters that were spectroscopically confirmed. These emitters were primarily $H\alpha$ and $[NII]$, all of which were removed from the sample. Our final sample consists of 307 $H\beta+[OIII]$ emitters at $z = 1.47$ that were selected.

A0.3 $H\beta+[OIII]$ & $[OII]$ Emitters at $z \sim 2.2$

$[OII]$ emitters in NBJ are selected if their photometric redshifts are between $1.7 < z_{phot} < 2.8$. We apply the BzK color-color selection to remove the lower- z contaminants, which are primarily $H\alpha$ emitters, as shown in figure A2. We then use the izK color-color selection to separate the sample from $H\beta+[OIII]$ emitters. There were no spectroscopically confirmed sources included in the sample. Removed from the sample were 3 contaminants, which were all low- z emitters (1 $[NII]$, 1 $[OIII]$, and 1 $[HeI]$). In total, there are 125 $[OII]$ emitters selected at $z = 2.23$.

$H\beta+[OIII]$ emitters at $z \sim 2.2$ in NBH are selected with photometric redshifts between $1.7 < z_{phot} < 2.8$ along with BzK and izK color-color selections. We apply the BzK color-color selection to remove emitters with $z \lesssim 1.5$ (primarily the $z = 1.47$ $H\alpha$ emitters) and then apply the izK

Table A1. Definitions of the Color-Color Selection

| Filter | Color-Color | Emitter | Redshift | Selection Criteria |
|--------|-------------|---------------------------|----------|---|
| NB921 | $BRiK$ | $H\beta+[OIII]$ | 0.84 | $-0.3 < (B - R) < 0.08 \& (i - K) < 2.04(B - R) + 0.81$ $0.08 < (B - R) < 1 \& 1.6(B - R) < (i - K) < 2.04(B - R) + 0.81$ $1 < (B - R) < 1.24 \& 1.6(B - R) < (i - K) < 3.21$ $1.24 < (B - R) \& 2.01 < (i - K) < 3.21$ $(B - R) < -0.3$ $-0.3 < (B - R) < 1.17 \& (i - K) > 2.04(B - R) + 0.81$ $(B - R) > 1.17 \& (i - K) > 3.21$ |
| | | $[OII]$ | 1.47 | |
| NBJ | BzK | $H\beta+[OIII]$ & $[OII]$ | | $(B - z) < 0.4$ $0.4 < (B - z) < 2.41 \& (z - K) > (B - z) - 0.4$ $2.41 < (B - z) \& (z - K) > 2.0$ |
| | | izK | 1.47 | $(z - K) < 5(i - z) - 0.4$ |
| NBH | BzK | $H\beta+[OIII]$ | 2.23 | $(B - z) < 0.4$ $0.4 < (B - z) < 2.41 \& (z - K) > (B - z) - 0.4$ $2.41 < (B - z) \& (z - K) > 2.0$ |
| | | izK | 2.23 | $(z - K) > 5(i - z) - 0.4$ |
| NBK | UVz | $H\beta+[OIII]$ | 3.3 | $(U - V) > 1.2 \& (U - V) > 0.5(V - z) + 1.2 \& (V - z) < 1.6$ |
| | | $[OII]$ | 4.7 | $(V - i) > 1.2 \& (V - i) > 0.89(i - z) + 1.2 \& (i - z) < 1.3$ |

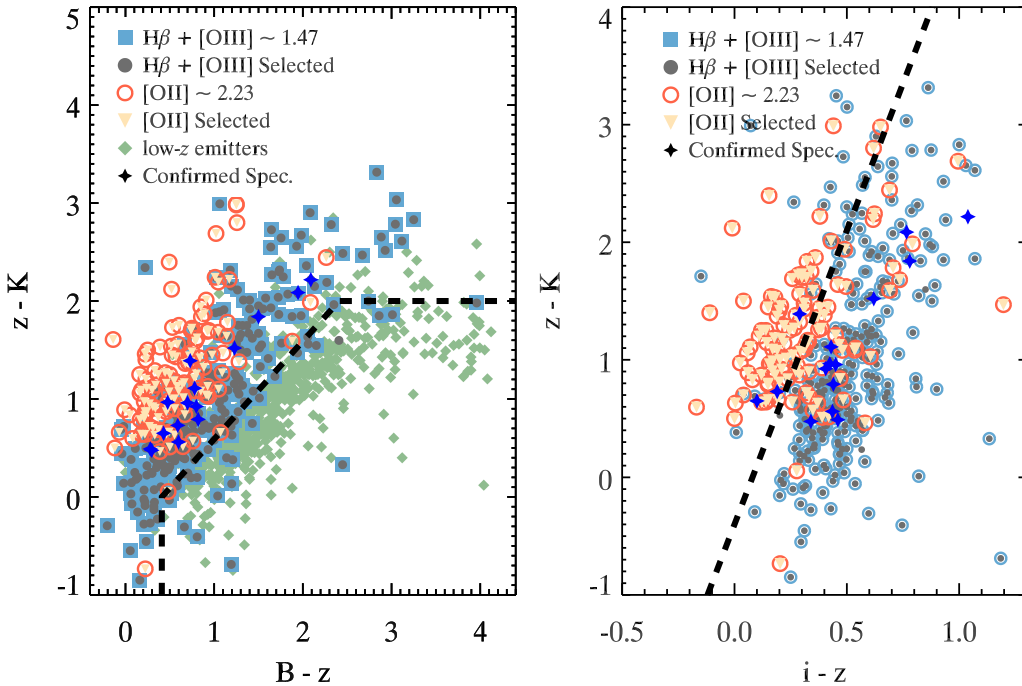


Figure A2. Color-color magnitude distributions for all NBJ emitters. *Left:* The $z - K$ versus $B - z$ selection used to separate the $H\beta+[OIII]$ emitters at $z \sim 1.47$ and $[OII]$ emitters at $z \sim 2.23$ from the low- z emitters that are primarily $H\alpha$. *Right:* The $z - K$ versus $i - z$ selection is used to select $[OII]$ and $H\beta+[OIII]$ emitters. For both selections, the spectroscopically confirmed emitters lie within the selection region adding to completeness of the sample. Both color-color selections nicely distinguish between the two samples. We note that for the izK selection, about $\sim 38\%$ of selected $[OII]$ emitters are within the selection region of $H\beta+[OIII]$ emitters. These are photo- z selected and shows that relying on purely the color-color selection would show a $\sim 38\%$ drop in the completeness of the $[OII]$ sample, and a $\sim 38\%$ increase in the contamination of the $H\beta+[OIII]$ sample.

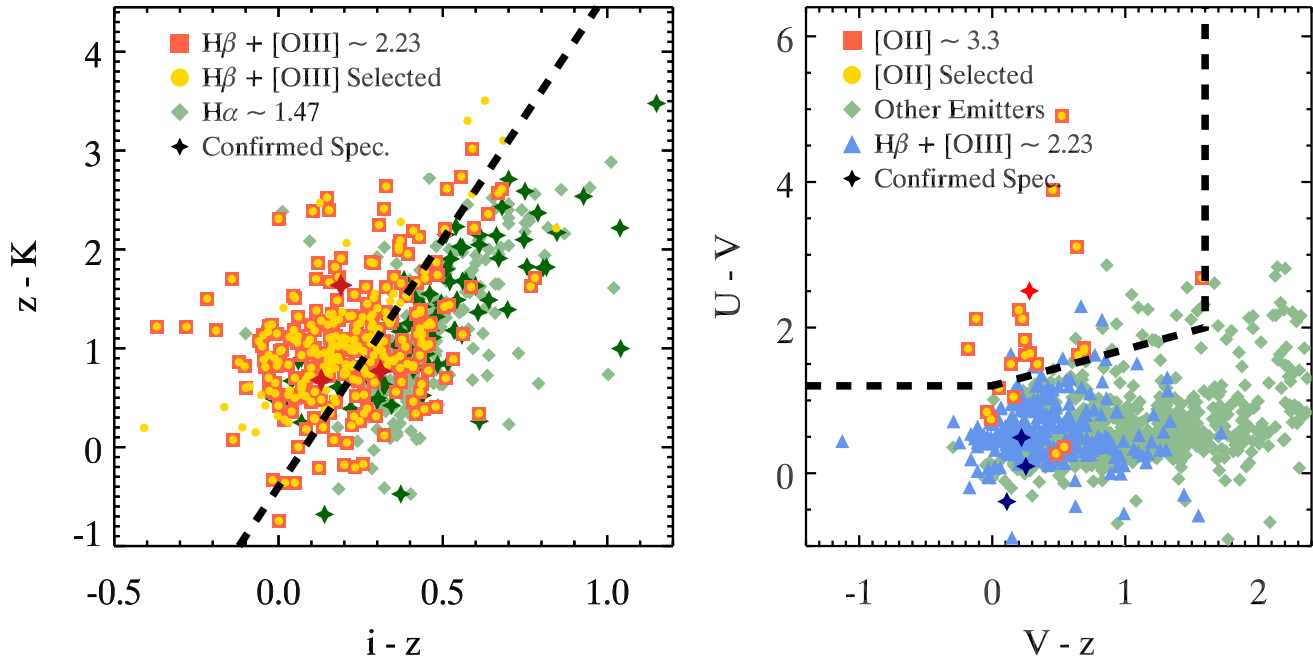


Figure A3. Color-color magnitude distributions of all NBH emitters. *Left:* The $z - K$ versus $i - z$ color-color selection used to separate the $H\beta + [OIII]$ $z \sim 2.23$ emitters from the $H\alpha$ $z \sim 1.47$ emitters (selected based on the methodology of Sobral et al. 2013). We have highlighted the spectroscopically confirmed emitters. The color-color selection shows a clear separation between $H\beta$ and $H\alpha$ measurements based on spectroscopic measurements alone. We find that 37% of our photo- z selected $H\beta + [OIII]$ emitters are within the selection area for $H\alpha$ emitter, showing that relying on just color-color selection would result in the loss of ~ 100 emitters from the sample and an increase in contamination of the $H\alpha$ sample. *Right:* The $U - V$ versus $V - z$ color-color selection that is based on the Lyman break drop-out technique and is used to find $z \sim 3.3$ $[OII]$ emitters. We also include the $H\beta + [OIII]$ sample and show that the vast majority of these emitters are outside the $[OII]$ color-color selection region.

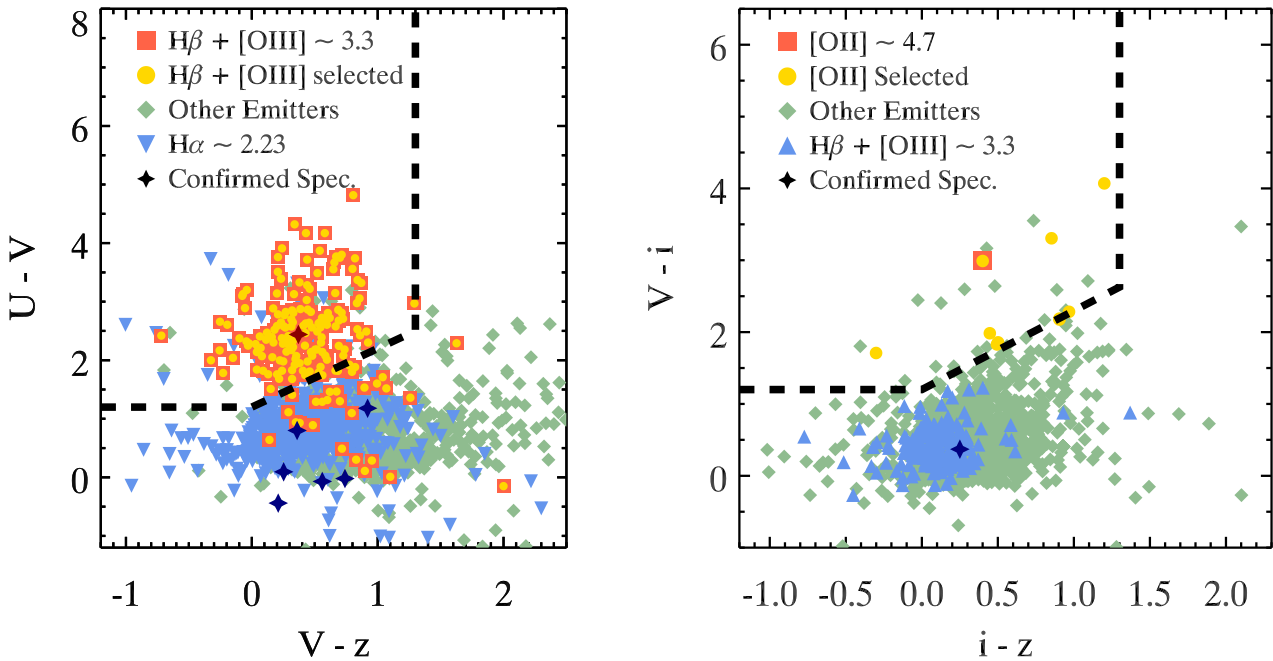


Figure A4. Color-color magnitude distributions of all NBK emitters. *Left:* shows the $U - V$ versus $V - z$ color-color selection used to find $z \sim 3.3$ $H\beta + [OIII]$ emitters based on the Lyman break drop-out technique. We also include the $H\alpha$ emitters ($z \sim 2.23$) and find that this selection reliably separates the two samples. *Right:* shows the $V - i$ versus $i - z$ color-color selection used to find $z \sim 4.7$ $[OII]$ emitters based also on the Lyman break drop-out technique. We include the $H\beta + [OIII]$ sample to show that this selection criteria is reliable to separate the two samples. We find no $H\beta + [OIII]$ emitter falling within the $[OII]$ color-color region.

color-color selection (shown in figure A3) to separate our $H\beta+[OIII]$ sample from the $z = 1.47$ $H\alpha$ emitters. We find that 37% of our sample is outside the color-color region in figure A3 but is still selected via the photo- z selection. This would raise concerns about the reliability of the color-color selection, but we must point out that it is reliable in terms of the separation between the $H\beta+[OIII]$ and $H\alpha$ spectroscopically confirmed emitters. This also raises the point that we are more concerned with consistency in the use of selection techniques to reduce the effects of assumptions in our sample. Furthermore, this also shows that we can not rely on the color-color selection technique alone to select emitters since this would result in a 37% drop in $H\beta+[OIII]$ emitters and a 37% increase in the contamination of the $H\alpha$ sample in Sobral et al. (2013). By including the photo- z in our selection methodology, we reduce the level of contaminants and also increase the reliability of the sample. We also included three spectroscopically confirmed sources in the sample that were selected by their color-color selection. Of these 3, we have two $[OIII]4959$ and one $[OIII]5007$ emitter. Removed from the sample were 3 low- z spectroscopically confirmed emitters ($H\alpha$ at $z \sim 1.47$). There were no high- z spectroscopic measurements that contaminated the sample. A total of 329 $H\beta+[OIII]$ emitters at $z = 2.23$ were selected.

A0.4 $H\beta+[OIII]$ & $[OII]$ Emitters at $z \sim 3.3$

$[OII]$ emitters at $z = 3.3$ in NBH are selected if $2.8 < z_{phot} < 4$. We also select sources if they satisfy the UVz color-color criteria. This separates the lower- z contaminants from our sample. We include our $H\beta+[OIII]$ sample in figure A3 to show the separation between the $[OII]$ and $H\beta+[OIII]$ sample and find that the UVz selection is reliable in selecting our $[OII]$ sample. Furthermore, as there are no major emission lines that are detected at higher- z , there is no need to include another color-color criteria to account for this contamination. As shown in fig. 2, the number of sources greatly drops at higher- z for the redshift of interest, making the number of contaminants very small. There was only one spectroscopically confirmed source that was included in the sample and only found in COSMOS. The UVz color of this emitter places it well within the selection area, adding to the reliability of our color-color selection. No spectroscopic confirmed emitters were misidentified in the selection. In total, there are 28 of $[OII]$ emitters at $z = 3.3$ selected.

Our $H\beta+[OIII]$ emitters at $z = 3.3$ in NBK are selected if their photometric redshifts lie between $2.8 < z_{phot} < 4$. We use a UVz selection criteria, as shown in figure A3, to select $H\beta+[OIII]$ emitters based on the Lyman break dropout technique. Sources with no detection bluer than the U -band and detection in the V and z bands greater than the 5σ magnitude detection limits were included. We also include all $H\alpha$ emitters with photo- z around $z = 2.23$ in figure A4 to show the separation between them and our $H\beta+[OIII]$ selected emitters. One spectroscopically confirmed source was also included in the sample from UDS. We find that this spectroscopically confirmed emitter is well within the color-color region. No spectroscopic confirmed emitters were misidentified in the selection. A total of 176 $H\beta+[OIII]$ emitters at $z = 3.3$ were selected.

A0.5 $[OII]$ emitters at $z \sim 4.7$

We select our $[OII]$ emitters in NBK if they have a photometric redshift between $4.0 < z_{phot} < 6.0$. Emitters are also selected by using the Viz criteria of Stark et al. (2009) for V -band dropouts. The color-color selection is shown in figure A4 and includes our $H\beta+[OIII]$ sample. We find that there are no $H\beta+[OIII]$ emitters within the $[OII]$ selection area, which adds to the reliability of our sample. We find only one emitter was selected by its photo- z within the selection range and it is well within the color-color selection region. The majority of emitters were selected by the color-color selection. All sources selected were also under the condition that anything bluer than V -band must have no detection. A study of $[OII]$ emitters by Bayliss et al. (2012) also used a similar technique using the BVz criteria of Stark et al. (2009) for their $z \sim 4.6$ sample. It must be noted though that the results of this study should not be taken as reliable due to the fact that they were limited to a sample size of only 3 $[OII]$ emitters (about 3 times smaller than our sample) and the volume probed by this study is a factor of 100 times smaller than our study making it severely susceptible to cosmic variance. Our sample is statistically larger and robust in comparison to Bayliss et al. (2012). There were no spectroscopically confirmed sources in our sample and no spectroscopic confirmed emitters were misidentified in the selection, thus, giving a total of 10 $[OII]$ emitters at $z = 4.5$ that were selected.

A0.6 Notes on Contamination

We advise the reader that the measurements of contamination are *not* strictly reliable for the $H\beta+[OIII]$ $z \sim 1.5$ emitters due to the bias in the spectroscopic redshift distribution. Two issues arise are: (1) lack of spectroscopic measurements at higher redshifts to properly quantify the level of contamination, and (2) the inherent bias of spectroscopic measurements to the lower- z regime. The first point really just requires more spectroscopic measurements to increase the population of spectroscopically confirmed sources. The second point has to do with the distribution of spec- z measurements. There exists more spec- z measurements for $z < 1$, which results in a skewed histogram that favors the lower- z regime. When measuring the level of contamination, there are more low- z measurements than spectroscopically confirmed measurements (for example, $z = 1.47$ $[OII]$) which causes a “naive” and biased estimation of the level of contamination. Instead, we considered where the spectroscopically confirmed $H\beta+[OIII]$ and $[OII]$ measurements were on the color-color diagrams as a way to assess the reliability of our selection technique.

Based on the points described above, we can measure the level of contamination for the $H\beta+[OIII]$ $z \sim 0.84$ sample ($\sim 10\%$). To robustly measure the contamination for the higher- z samples, we will need to conduct spectroscopic follow-up which is currently underway with Keck/MOSFIRE and ESO/VLT (Khstovan et al., in prep).

Table B1. $H\beta+[\text{OIII}]$ Luminosity Function. Φ_{obs} shows the observed LF data points per bin; simply, it is the log of the number of emitters divided by the volume. Φ_{final} is the completeness and filter profile corrected luminosity data points per bin. The errors here are Poissonian but with 20% of the corrections added in quadrature.

| $\log_{10} L_{H\beta+[\text{OIII}]}$ (erg s $^{-1}$) | # | Φ_{obs} (Mpc $^{-3}$ d log $_{10}$ L) | Φ_{final} (Mpc $^{-3}$ d log $_{10}$ L) | Volume (10 5 Mpc 3) |
|--|-----|--|--|-------------------------------|
| $z = 0.84$ | | | | |
| 41.00 ± 0.05 | 282 | -2.06 | -1.86 ± 0.03 | 3.25 |
| 41.10 ± 0.05 | 372 | -1.94 | -1.72 ± 0.03 | 3.25 |
| 41.20 ± 0.05 | 302 | -2.03 | -1.89 ± 0.03 | 3.25 |
| 41.30 ± 0.05 | 232 | -2.15 | -2.01 ± 0.04 | 3.25 |
| 41.40 ± 0.05 | 197 | -2.22 | -2.11 ± 0.04 | 3.25 |
| 41.50 ± 0.05 | 137 | -2.37 | -2.31 ± 0.05 | 3.25 |
| 41.60 ± 0.05 | 92 | -2.55 | -2.43 ± 0.07 | 3.25 |
| 41.70 ± 0.05 | 61 | -2.73 | -2.63 ± 0.08 | 3.25 |
| 41.80 ± 0.05 | 55 | -2.77 | -2.63 ± 0.09 | 3.25 |
| 41.90 ± 0.05 | 23 | -3.15 | -3.06 ± 0.14 | 3.25 |
| 42.00 ± 0.05 | 27 | -3.08 | -2.92 ± 0.13 | 3.25 |
| 42.10 ± 0.05 | 15 | -3.34 | -3.16 ± 0.17 | 3.25 |
| 42.20 ± 0.05 | 10 | -3.51 | -3.41 ± 0.21 | 3.25 |
| 42.30 ± 0.05 | 6 | -3.73 | -3.30 ± 0.28 | 3.25 |
| 42.40 ± 0.05 | 4 | -3.91 | -3.66 ± 0.34 | 3.25 |
| 42.50 ± 0.05 | 1 | -4.51 | -4.11 ± 0.68 | 3.25 |
| $z = 1.42$ | | | | |
| 41.95 ± 0.15 | 222 | -2.73 | -2.57 ± 0.03 | 3.94 |
| 42.25 ± 0.15 | 69 | -3.25 | -3.15 ± 0.07 | 4.06 |
| 42.55 ± 0.15 | 10 | -4.09 | -3.97 ± 0.21 | 4.06 |
| 42.85 ± 0.15 | 2 | -4.78 | -4.63 ± 0.48 | 4.06 |
| $z = 2.23$ | | | | |
| 42.60 ± 0.10 | 124 | -3.23 | -3.03 ± 0.05 | 10.46 |
| 42.80 ± 0.10 | 90 | -3.38 | -3.13 ± 0.06 | 10.69 |
| 43.00 ± 0.10 | 16 | -4.13 | -3.87 ± 0.16 | 10.69 |
| $z = 3.24$ | | | | |
| 42.65 ± 0.10 | 77 | -3.37 | -3.22 ± 0.07 | 9.11 |
| 42.85 ± 0.10 | 59 | -3.53 | -3.34 ± 0.08 | 9.94 |
| 43.05 ± 0.10 | 7 | -4.48 | -4.21 ± 0.25 | 10.48 |
| 43.25 ± 0.10 | 1 | -5.32 | -4.85 ± 0.68 | 10.48 |

APPENDIX B: BINNED LUMINOSITY FUNCTION

Here we include two tables that show the binned data points of the LF that are plotted in figures 4 and 6. We include these plots as a convenience for future studies who wish to compare their LFs to ours.

APPENDIX C: STAR-FORMATION RATE DENSITY COMPILATION

In this section, we have compiled a table of the star-formation rate densities from different diagnostics spread over a wide redshift range. Because each study has its own set of assumptions, diagnostics, calibrations, dust corrections,etc. it is quite confusing in keeping track of which study has used which set of assumptions. Let alone, for the earliest papers, we have to even take into account the different cosmologies. To make life much easier for you as the reader who may be interested in studying the evolution of the cosmic SFR density, we have included in the appendix a long table which is our compilation of the SFR densities and luminosity function parameters from a range of different studies. Parts of this table are from Ly et al. (2007), but updated with the newest studies in the field.

Table B2. $[\text{OII}]$ Luminosity Function. Φ_{obs} shows the observed LF data points per bin; simply, it is the log of the number of emitters divided by the volume. Φ_{final} is the completeness and filter profile corrected luminosity data points per bin. The errors here are Poissonian but with 20% of the corrections added in quadrature.

| $\log_{10} L_{[\text{OII}]}$ (erg s $^{-1}$) | # | Φ_{obs} (Mpc $^{-3}$ d log $_{10}$ L) | Φ_{final} (Mpc $^{-3}$ d log $_{10}$ L) | Volume (10 5 Mpc 3) |
|--|-----|--|--|-------------------------------|
| $z = 1.47$ | | | | |
| 41.10 ± 0.05 | 188 | -2.16 | -1.93 ± 0.03 | 2.75 |
| 41.20 ± 0.05 | 478 | -1.90 | -1.66 ± 0.02 | 3.77 |
| 41.30 ± 0.05 | 389 | -2.09 | -1.90 ± 0.02 | 4.78 |
| 41.40 ± 0.05 | 333 | -2.24 | -2.11 ± 0.02 | 5.78 |
| 41.50 ± 0.05 | 276 | -2.39 | -2.18 ± 0.03 | 6.80 |
| 41.60 ± 0.05 | 344 | -2.30 | -2.12 ± 0.03 | 6.80 |
| 41.70 ± 0.05 | 367 | -2.27 | -2.15 ± 0.03 | 6.80 |
| 41.80 ± 0.05 | 264 | -2.41 | -2.26 ± 0.04 | 6.80 |
| 41.90 ± 0.05 | 213 | -2.50 | -2.40 ± 0.04 | 6.80 |
| 42.00 ± 0.05 | 113 | -2.78 | -2.52 ± 0.06 | 6.80 |
| 42.10 ± 0.05 | 91 | -2.87 | -2.66 ± 0.07 | 6.80 |
| 42.20 ± 0.05 | 42 | -3.21 | -3.07 ± 0.10 | 6.80 |
| 42.30 ± 0.05 | 23 | -3.47 | -3.10 ± 0.14 | 6.80 |
| 42.40 ± 0.05 | 8 | -3.93 | -3.53 ± 0.24 | 6.80 |
| 42.50 ± 0.05 | 5 | -4.13 | -3.83 ± 0.30 | 6.80 |
| 42.60 ± 0.05 | 2 | -4.53 | -4.53 ± 0.48 | 6.80 |
| $z = 2.25$ | | | | |
| 42.45 ± 0.05 | 66 | -2.98 | -2.79 ± 0.07 | 6.29 |
| 42.55 ± 0.10 | 47 | -3.13 | -2.89 ± 0.08 | 6.29 |
| 42.75 ± 0.10 | 12 | -4.20 | -3.99 ± 0.18 | 6.29 |
| $z = 3.34$ | | | | |
| 42.95 ± 0.05 | 17 | -3.95 | -3.64 ± 0.13 | 15.24 |
| 43.05 ± 0.05 | 11 | -4.16 | -3.84 ± 0.18 | 15.88 |
| 43.15 ± 0.05 | 6 | -4.44 | -4.11 ± 0.26 | 16.52 |
| 43.25 ± 0.05 | 1 | -5.22 | -4.92 ± 0.68 | 16.52 |
| $z = 4.69$ | | | | |
| 42.83 ± 0.08 | 5 | -4.59 | -3.83 ± 0.11 | 12.22 |
| 42.99 ± 0.08 | 4 | -4.69 | -3.93 ± 0.13 | 12.22 |
| 43.15 ± 0.08 | 1 | -5.29 | -4.32 ± 0.22 | 12.22 |

This paper has been typeset from a $\text{TeX}/\text{\LaTeX}$ file prepared by the author.

Table C1. SFRD Compilation

| Study | z | Diagnostic | Observed | | | $\log_{10} \dot{\rho}_*$ $M_{\odot} \text{ yr}^{-1} \text{ Mpc}^{-3}$ |
|-------------------------------|-------------------|------------|---|--|-------------------------|--|
| | | | $\log_{10} \phi_*$ Mpc^{-3} | $\log_{10} L_*$ erg s^{-1} | α | |
| Ciardullo et al. 2013 | 0.0 – 0.2 | [OII] | $-2.30^{+0.09}_{-0.11}$ | $40.32^{+0.18}_{-0.16}$ | -1.2 | -2.05 ± 0.11 |
| | 0.2 – 0.325 | [OII] | $-2.12^{+0.05}_{-0.06}$ | 40.54 ± 0.11 | -1.2 | -1.82 ± 0.06 |
| | 0.325 – 0.45 | [OII] | $-2.07^{+0.04}_{-0.05}$ | $40.75^{+0.08}_{-0.10}$ | -1.2 | -1.71 ± 0.05 |
| | 0.45 – 0.56 | [OII] | $-2.07^{+0.03}_{-0.08}$ | $40.93^{+0.08}_{-0.12}$ | -1.2 | -1.66 ± 0.06 |
| Sobral et al. 2012 | 1.47 | [OII] | -2.01 ± 0.10 | 41.71 ± 0.09 | -0.9 ± 0.2 | -1.48 ± 0.10 |
| Bayliss et al. 2011 | 1.85 | [OII] | -2.23 ± 0.09 | 41.31 ± 0.06 | -1.3 ± 0.2 | -0.92 ± 0.08 |
| Ly et al. 2007 | 0.89 | [OII] | -2.25 ± 0.13 | 41.33 ± 0.09 | -1.27 ± 0.14 | -1.68 ± 0.03 |
| | 0.91 | [OII] | -1.97 ± 0.09 | 41.40 ± 0.07 | -1.20 ± 0.10 | -1.36 ± 0.02 |
| | 1.18 | [OII] | -2.20 ± 0.10 | 41.74 ± 0.07 | -1.15 ± 0.11 | -1.27 ± 0.02 |
| | 1.47 | [OII] | -1.97 ± 0.06 | 41.60 ± 0.05 | -0.78 ± 0.13 | -1.27 ± 0.02 |
| Zhu, Moustakas & Blanton 2009 | 0.84 | [OII] | ... | ... | ... | $-1.79^{+0.10}_{-0.10}$ |
| | 1.02 | [OII] | ... | ... | ... | $-1.75^{+0.13}_{-0.08}$ |
| | 1.19 | [OII] | ... | ... | ... | $-1.67^{+0.25}_{-0.11}$ |
| | 1.37 | [OII] | ... | ... | ... | $-1.60^{+0.16}_{-0.09}$ |
| Takahashi et al. 2007 | 1.71 – 1.203 | [OII] | $-2.37^{+0.10}_{-0.12}$ | $41.79^{+0.07}_{-0.06}$ | $-1.41^{+0.16}_{-0.15}$ | $-1.25^{+0.05}_{-0.08}$ |
| | 1.71 – 1.203 | [OII] | $-2.67^{+0.28}_{-0.49}$ | $41.75^{+0.32}_{-0.20}$ | $-1.38^{+0.40}_{-0.37}$ | $-1.61^{+0.09}_{-0.28}$ |
| Glazebrook et al. 2004 | 0.90 | [OII] | -2.91 | 42.30 | -1.3 | $-1.35^{+0.34}_{-0.30}$ |
| Teplitz et al. 2003 | 0.90 \pm 0.50 | [OII] | -3.06 ± 0.12 | 42.15 ± 0.08 | -1.35 | -1.55 ± 0.06 |
| Gallego et al. 2002 | 0.025 \pm 0.025 | [OII] | -3.48 ± 0.19 | 41.24 ± 0.13 | -1.21 ± 0.21 | -3.02 ± 0.15 |
| Hicks et al. 2002 | 1.20 \pm 0.40 | [OII] | ... | ... | ... | $-1.59^{+0.30}_{-0.48}$ |
| Hogg et al. 1998 | 0.20 \pm 0.10 | [OII] | ... | ... | ... | $-2.37^{+0.11}_{-0.16}$ |
| | 0.40 \pm 0.10 | [OII] | ... | ... | ... | $-1.77^{+0.09}_{-0.12}$ |
| | 0.60 \pm 0.10 | [OII] | ... | ... | ... | $-1.69^{+0.06}_{-0.08}$ |
| | 0.80 \pm 0.10 | [OII] | ... | ... | ... | $-1.75^{+0.07}_{-0.08}$ |
| | 1.00 \pm 0.10 | [OII] | ... | ... | ... | $-1.44^{+0.09}_{-0.11}$ |
| | 1.20 \pm 0.10 | [OII] | ... | ... | ... | $-1.57^{+0.18}_{-0.30}$ |
| | 0.375 \pm 0.125 | [OII] | ... | ... | ... | $-2.20^{+0.07}_{-0.08}$ |
| Hammer et al. 1997 | 0.625 \pm 0.125 | [OII] | ... | ... | ... | $-1.72^{+0.11}_{-0.15}$ |
| | 0.875 \pm 0.125 | [OII] | ... | ... | ... | $-1.35^{+0.20}_{-0.38}$ |
| | 0.7 – 1.5 | [OIII] | -3.19 ± 0.09 | 42.34 ± 0.06 | -1.40 ± 0.15 | ... |
| Colbert et al. 2013 | 1.5 – 2.3 | [OIII] | -3.74 ± 0.43 | 42.91 ± 0.37 | -1.67 ± 0.78 | ... |
| | 0.7 – 1.5 | [OIII] | -3.28 ± 0.09 | 42.39 ± 0.08 | -1.50 | ... |
| | 1.5 – 2.3 | [OIII] | -3.60 ± 0.14 | 42.83 ± 0.11 | -1.50 | ... |
| | 0.5 \pm 0.4 | [OIII] | $-2.58^{+0.09}_{-0.09}$ | $41.3^{+0.09}_{-0.09}$ | $-1.21^{+0.08}_{-0.07}$ | ... |
| Pirzkal et al. 2013 | 0.41 | [OIII] | -2.55 ± 0.25 | 41.17 ± 0.22 | -1.49 ± 0.11 | -2.17 ± 0.06 |
| | 0.42 | [OIII] | -2.38 ± 0.22 | 41.11 ± 0.24 | -1.25 ± 0.13 | -2.31 ± 0.09 |
| | 0.62 | [OIII] | -2.58 ± 0.17 | 41.51 ± 0.15 | -1.22 ± 0.13 | -2.06 ± 0.05 |
| | 0.83 | [OIII] | -2.54 ± 0.15 | 41.53 ± 0.11 | -1.44 ± 0.09 | -1.73 ± 0.03 |